CANCER

Targeting conserved TIM3$^+$VISTA$^+$ tumor-associated macrophages overcomes resistance to cancer immunotherapy

Isaure Vanmeerbeek[1], Stefan Naulaerts[1], Jenny Sprooten[1], Raquel S. Laureano[1], Jannes Govaerts[1], Rosa Trotta[2,3], Samantha Pretto[2,3], Shikang Zhao[2,3], Sarah Trusso Cafarello[2,3], Joren Verelst[2,3], Maarten Jacquemyn[4], Martyna Pociupany[1], Louis Boon[5], Susan M. Schlenner[6], Sabine Tejpar[7], Dirk Daelemans[4], Massimiliano Mazzone[2,3], Abhishek D. Garg[1]*

Despite the success of immunotherapy, overcoming immunoresistance in cancer remains challenging. We identified a unique niche of tumor-associated macrophages (TAMs), coexpressing T cell immunoglobulin and mucin domain–containing 3 (TIM3) and V-domain immunoglobulin suppressor of T cell activation (VISTA), that dominated human and mouse tumors resistant to most of the currently used immunotherapies. TIM3$^+$VISTA$^+$ TAMs were sustained by IL-4–enriching tumors with low (neo)antigenic and T cell–depleted features. TIM3$^+$VISTA$^+$ TAMs showed an anti-inflammatory and protumorigenic phenotype coupled with inability to sense type I interferon (IFN). This was established with cancer cells succumbing to immunogenic cell death (ICD). Dying cancer cells not only triggered autocrine type I IFNs but also exposed HMGB1/VISTA that engaged TIM3/VISTA on TAMs to suppress paracrine IFN-responses. Accordingly, TIM3/VISTA blockade synergized with paclitaxel, an ICD-inducing chemotherapy, to repolarize TIM3$^+$VISTA$^+$ TAMs to proinflammatory TAMs that killed cancer cells via tumor necrosis factor–related apoptosis-inducing ligand (TRAIL) signaling. We propose targeting TIM3$^+$VISTA$^+$ TAMs to overcome immunoresistant tumors.

INTRODUCTION

Immune checkpoint signaling, involving interactions between inhibitory receptors and their ligands, is used by tumors to suppress anticancer immunity (*1*). Accordingly, immune checkpoint blockers (ICBs) targeting "classical" inhibitory receptors on T cells [such as programmed cell death protein 1 (PD1)] or their ligands [such as programmed cell death protein ligand 1 (PD-L1)] have revolutionized oncology (*2*). Regrettably, several tumor types remain unresponsive to PD(L)1 blockade (*3*, *4*). These immunoresistant tumors typically show low antigenicity and sparse T cells but enrichment of tumor-associated macrophages (TAMs) (*5*). Some of the most dominant immunoresistance mechanisms include defects in antigen presentation or availability, TAM-based immunosuppression, dysregulated interferon-γ (IFN-γ) signaling, or enrichment of alternative inhibitory receptors (*4*, *6*). Currently, substantial research is devoted to overcoming these barriers; however, this pursuit has also revealed some challenges (*3*, *4*). For instance, in some cases, coblockade of alternative inhibitory receptors along with PD1 has shown promise, e.g., coblockade of lymphocyte-activation gene 3 (LAG3) and PD1 (*7*, *8*). However, in other cases, blockade of T cell immunoglobulin and mucin domain–containing 3 (TIM3), T cell immunoreceptor with immunoglobulin and immunoreceptor tyrosine-based inhibitory motif domains (TIGIT), or V-domain immunoglobulin suppressor of T cell activation (VISTA) has had mixed or disappointing early clinical performance (*8*–*10*).

Most studies targeting inhibitory receptors concentrate on T cells (*11*, *12*). While, previously, this association was considered to be exclusive, it has recently been extended to TAMs (*13*, *14*). However, the immunobiology of TAM-specific inhibitory receptors enriched in immunoresistant tumors, and their therapeutic or clinical impact remains unexplored. This requires urgent attention because high enrichment of TAMs can facilitate overrepresentation of this inhibitory receptor signaling (*15*). However, it is not clear which classical or alternative inhibitory receptors are preferentially exploited by TAMs to support immune subversion. In addition, it is essential to understand whether these TAMs are conserved across both human and mouse contexts (*16*).

Here, using reverse translational approaches, we identified a niche of TIM3$^+$VISTA$^+$ TAMs that dominated the human and mouse immunoresistant (CD8$^+$ T cell sparse) tumors. Both TIM3 and VISTA were instrumental to sustain an anti-inflammatory and protumorigenic TAM phenotype and to blunt type I IFN signaling. Accordingly, TIM3/VISTA blockade preferentially synergized with chemotherapy that induced type I IFN signaling via immunogenic cell death (ICD). This combinatorial regimen helped replace the anti-inflammatory footprint of TIM3$^+$VISTA$^+$ TAMs with a proinflammatory TAM phenotype. These TAMs drove anticancer cytotoxicity via tumor necrosis factor (TNF)–related apoptosis-inducing ligand (TRAIL) signaling, thereby blunting the immunoresistant tumors. This therapeutic synergism is peculiar because it triggered TAM autonomous control of tumor growth, independent of CD8$^+$ T cells or dendritic cells (DCs). These results are important because, in the current literature, the therapeutic efficacy of TIM3/VISTA blockade, irrespective of their myeloid or T cell expression, always converges on CD8$^+$ T cell–driven tumor control (*17*–*19*). Last, genetic footprint of TIM3$^+$VISTA$^+$ TAMs

---

[1]Laboratory of Cell Stress and Immunity, Department of Cellular and Molecular Medicine, KU Leuven, Leuven, Belgium. [2]Laboratory of Tumour Inflammation and Angiogenesis, VIB Center for Cancer Biology, Leuven, Belgium. [3]Laboratory of Tumour Inflammation and Angiogenesis, Department of Oncology, KU Leuven, Leuven, Belgium. [4]Laboratory of Virology and Chemotherapy, Department of Microbiology, Immunology and Transplantation, KU Leuven, Rega Institute, Leuven, Belgium. [5]JJP Biologics, Warsaw, Poland. [6]Laboratory of Adaptive Immunity, Department of Microbiology, Immunology and Transplantation, KU Leuven, Leuven, Belgium. [7]Laboratory for Molecular Digestive Oncology, Department of Oncology, KU Leuven, Leuven, Belgium.
*Corresponding author. Email: abhishek.garg@kuleuven.be

exhibited pan-cancer negative prognostic and predictive impact. Thus, targeting TIM3$^+$VISTA$^+$ TAMs is a conserved strategy to overcome low antigenic tumors.

RESULTS

HAVCR2$^+$*VSIR*$^+$TAMs specifically associate with immunoresistant human tumors

First, we set to identify the dominant inhibitory receptor(s) enriched in the myeloid cells or macrophages (MΦ) associated with ICB-nonresponsive human tumors. We assembled a comprehensive computational framework (*20*–*22*) integrating existing patient cohorts with single-cell RNA sequencing (scRNA-seq) data. This entailed supervised exploratory analyses across 114 patients, 11 tumor types, and 36 distinct scRNA-seq cohorts, as well as unsupervised validation analyses across ~300 human scRNA-seq cohorts, >15 million single cells, and >60 organ/disease contexts including cancer (Fig. 1A).

We compared the expression of nine major inhibitory receptor–coding genes (*NT5E*, *VSIR*, *ADORA2A*, *CTLA4*, *LAG3*, *HAVCR2*, *ENTPD1*, *PDCD1*, and *TIGIT*) (*20*, *23*) and a broad TAM marker (*CSF1R*), in T cells versus myeloid cells from patients with melanoma (*24*). These patients were either responsive or nonresponsive to anti-PD1/anti–cytotoxic T-lymphocyte associated protein 4 (CTLA4) ICBs. T cells from ICB-nonresponsive patients showed increased expression of multiple inhibitory receptor genes (Fig. 1B). However, myeloid cells showed enrichment of specifically two inhibitory receptor genes: *HAVCR2* (codes for TIM3) and *VSIR* (codes for VISTA), along with *CSF1R* (Fig. 1C). This coexpression of *HAVCR2* and *VSIR* was specific for TAMs and was not seen in other T or B cell subsets and DCs (fig. S1A).

To verify whether TAM-specific coenrichment of *HAVCR2*/*VSIR* was generalizable to other tumors, we used a multicancer and multi-immune cell scRNA-seq dataset (Fig. 1A) (*25*). A strong *HAVCR2*$^+$*VSIR*$^+$ phenotype was associated mainly with TAMs (Fig. 1D). This was not evident in DCs (fig. S1B), CD4$^+$/CD8$^+$ T cells, B cells, monocytes, or natural killer (NK) cells (Fig. 1D and fig. S1B). While interesting, in above analyses, the subpopulation diversity of TAMs, DCs, or monocytes was not captured. To ameliorate this, we used a larger multicancer and multimyeloid cell scRNA-seq meta-dataset (Fig. 1A) (*26*). Here, the *HAVCR2*^{HIGH}*VSIR*^{HIGH} phenotype was dominantly associated with *CSF1R*^{HIGH}TAMs, rather than other subsets of TAMs, DCs, or monocytes (Fig. 1E).

Above results called for more "controlled" analyses on how *HAVCR2*$^+$*VSIR*$^+$TAMs associate with immunogenic versus non-immunogenic tumors. To address this in a singular cancer type, we used a scRNA-seq dataset of patients with colorectal cancer (CRC) (Fig. 1A). This is because CRC tumors exhibit either immunogenic [i.e., microsatellite instable (MSI)] or nonimmunogenic [i.e., microsatellite stable (MSS)] pathologies (*27*). Data of normal adjacent tissue–associated MΦs were also interrogated. *HAVCR2*$^+$*VSIR*$^+$ phenotype was strongly associated with anti-inflammatory *SPP1*$^+$TAMs in MSS-CRC (Fig. 1F), rather than proinflammatory (S100A8/9^{HIGH}) TAMs or MSI-CRC (Fig. 1F) (*28*). A differential pathway enrichment analysis between *HAVCR2*$^+$*VSIR*$^+$ and *HAVCR2*^{NEG}*VSIR*^{NEG}TAMs showed that *HAVCR2*$^+$*VSIR*$^+$TAMs are enriched for phagocytosis, pattern recognition receptor (PRR) signaling relevant for danger sensing (e.g., nucleic acids), and anti-inflammatory signaling (Fig. 1G and fig. S1, C and D). These comprehensive single-cell analyses indicated that the *HAVCR2*$^+$*VSIR*$^+$TAM niche is preferentially enriched in immunoresistant human tumors.

HAVCR2 and *VSIR* comark a distinct anti-inflammatory MΦ subset in humans

Next, we wanted to verify whether *HAVCR2* and *VSIR* mark a distinct subset of MΦs/TAMs and how they associate with different MΦ subsets or polarization markers. Therefore, we performed an unbiased bioinformatics analysis across 2,489,382 MΦs from 1679 scRNA-seq studies of human origin (pan-disease or pan-tissue) with 26 markers of different MΦ subsets or polarization states (Fig. 2A) (*29*–*34*). This analysis revealed that *HAVCR2*$^+$ *VSIR*$^+$MΦs are indeed a distinct subset, and they did not overlap with many well-established markers of other MΦ subsets such as *IL10*, *ARG1*, *LYVE1*, *FOLR2*, *CCL2*, and *CR1* (Fig. 2A). Instead, the *HAVCR2*$^+$ *VSIR*$^+$MΦs were coclustered with primarily anti-inflammatory polarization markers, e.g., *CSF1R*, *CD163*, *MRC1*, *TREM2*, and *SPP1*. Notably, ~31% of the MΦs coexpressed *HAVCR2* and *VSIR* (fig. S1E).

Last, we validated the above results in an unbiased analysis. Here, we used an automated cell ontology analysis that used above *HAVCR2*$^+$ *VSIR*$^+$TAM signature (Fig. 1G) as a guide to find similar immune populations in a massive database of ~300 publicly available scRNA-seq datasets spanning >60 normal or diseased tissues (*35*). Notably, the alignment between *HAVCR2*$^+$ *VSIR*$^+$TAM signature and MΦs was a dominant characteristic of multiple human tumors (especially of epithelial origin), rather than other healthy/diseased tissues (Fig. 2B). Together, this emphasized that coexpression of *HAVCR2* and *VSIR* marks a distinct MΦ or TAM subset.

TIM3$^+$VISTA$^+$ TAM signature shows prognostic and predictive impact in patients with cancer

It was essential to verify how TIM3$^+$VISTA$^+$ TAMs embed in the human pan-cancer immune landscape and how they prognostically or predictively associate with patient survival. For this, we pursued a high-powered bulk tumor transcriptome mapping (Fig. 2C).

The Cancer Genome Atlas (TCGA) consortium has established six pan-cancer immune landscape classes (C1 to C6; for class labels, see radar plot in Fig. 2D) (fig. S2, A and B, and table S1) (*36*). We analyzed the correlation of immune-deconvoluted MΦ fractions, from above classes, with our scRNA-seq–validated *HAVCR2*$^+$ *VSIR*$^+$TAM signature in 8549 patients across 30 cancer types. The more immunoresistant C4/C5 tumors showed the highest correlation between *HAVCR2*$^+$ *VSIR*$^+$TAM signature and MΦs, followed by mixed inflammatory C3 tumors (Fig. 2D). In terms of prognostic impact, *HAVCR2*$^+$ *VSIR*$^+$TAM signature associated with increased hazard ratio (HR > 1) implying shorter overall survival (OS) in various pan-cancer immune landscape classes, with the only exception being the immunogenic IFN-γ–dominant tumors (Fig. 2E). Next, we interrogated an integrated multicancer dataset spanning five cancer types in patients, whose tumors were transcriptome-profiled relative to PD(L)1 and/or CTLA4 blockade (Fig. 2C). OS and progression-free survival (PFS) of *HAVCR2*$^+$ *VSIR*$^+$TAM signature^{HIGH} patients were significantly shorter than *HAVCR2*$^+$ *VSIR*$^+$TAM signature^{LOW} patients (Fig. 2, F and G). This highlighted a pan-cancer association of the *HAVCR2*$^+$ *VSIR*$^+$TAM signature with nonimmunogenic human tumors and its ability to predict shorter patient survival in prognostic and ICB response–predictive settings.

TIM3$^+$VISTA$^+$ TAMs are dominantly enriched in an immunoresistant murine tumor

To reverse translate above results, we needed unbiased selection of immunogenic versus nonimmunogenic murine tumor models. Hence, we

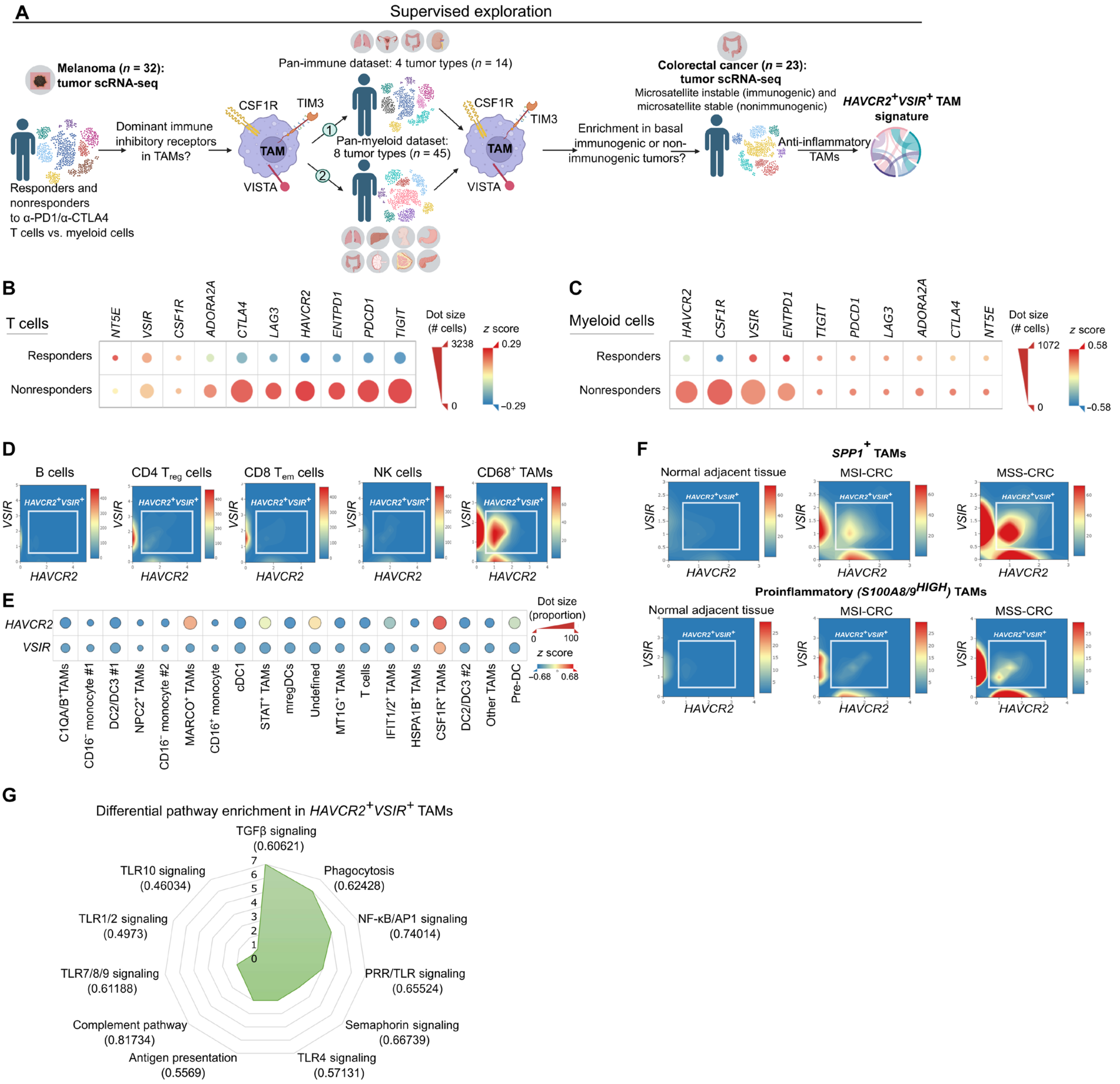

Fig. 1. *HAVCR2*$^+$*VSIR*$^+$ TAMs are specifically associated with immunoresistant human tumors. (**A**) Overview of our computational framework for single-cell transcriptome mapping based on existing datasets with patient-derived tumor tissue (created with BioRender.com). (**B** and **C**) Dot plots of scRNA-seq data from patients with skin cutaneous melanoma ($n = 32$) responding or not responding to PD1/CTLA4 blockade. Size of dots represents number of cells, and color intensity represents expression levels of indicated genes in single-cell profiles of (B) T cells and (C) myeloid cells. (**D**) Density plots of scRNA-seq data from 14 treatment-naive patients across four different types of cancer (lung, endometrial, and colorectal adenocarcinoma and clear cell renal cell carcinoma) showing *HAVCR2* and *VSIR* expression in indicated immune cell types. T$_{\text{reg}}$, regulatory T cell; T$_{\text{em}}$, effector memory T cell. (**E**) Dot plots of 33 scRNA-seq datasets including eight cancer types (non–small cell lung, head and neck, colorectal, stomach, breast, and pancreas cancer, hepatocellular carcinoma, and lymphoma) ($n = 45$). Size of dots represents number of cells, and color intensity represents expression levels of indicated genes in single-cell profiles in indicated immune cell types. mreg, mature regulatory. (**F**) Density plots of scRNA-seq data from 23 patients with primary colorectal cancer (CRC) [4 microsatellite instable (MSI) high and 19 microsatellite stable (MSS)] including 10 matched normal adjacent tissues, showing *HAVCR2* and *VSIR* expression in *SPP1*$^+$ TAMs and S100A8/9$^{\text{HIGH}}$ TAMs. (**G**) Aggregated scores for representative pathway terms based on a broader differential pathway enrichment analysis between *HAVCR2*$^+$*VSIR*$^+$TAMs versus *HAVCR2*$^{\text{NEG}}$*VSIR*$^{\text{NEG}}$TAMs in dataset from (F). Full differential pathway enrichment analysis in fig. S1 (C and D). AP1, activating protein 1.

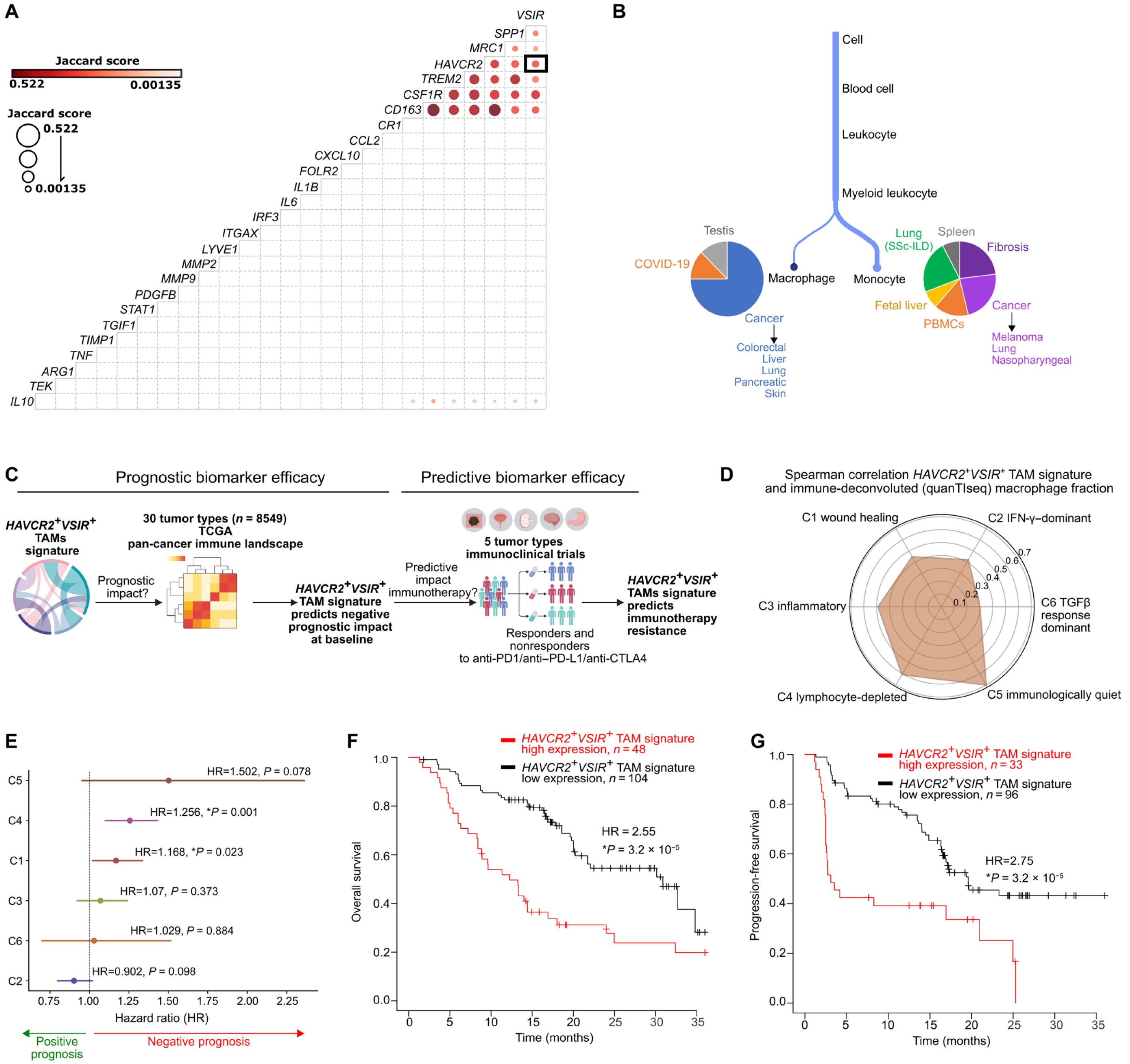

Fig. 2. TIM3$^+$VISTA$^+$ TAM signature shows prognostic and predictive impact in patients with cancer. (**A**) Coexpression of indicated genes' correlation (Jaccard's index) among themselves in scRNA-seq profiles of 2,489,382 MΦs from 1679 scRNA-seq studies of human origin (pan-disease or pan-tissue). (**B**) Automated cell ontology analyses run on an existing database of ~300 scRNA-seq human datasets interrogated using a genetic signature of *HAVCR2*$^+$*VSIR*$^+$TAMs derived from Fig. 1F. Final datasets were selected as "hits" based on a high Jaccard's index threshold of 0.7. (**C**) Overview of the high-powered bulk tumor transcriptome and high-resolution scRNA-seq mapping pipeline that was used for prognostic and predictive validation of our biomarker (created with BioRender.com). (**D**) Radar plot showing the correlation of immune-deconvoluted MΦ fractions with the scRNA-seq–validated *HAVCR2*$^+$*VSIR*$^+$ TAM signature in TCGA datasets consisting of six pan-cancer immune landscape classes (C1, n = 2067; C2, n = 2424, C3, n = 2349; C4, n = 1142, C5, n = 387; C6, n = 180) (for more details, see fig. S2, A and B, and table S1). (**E**) Hazard ratios (HRs) for the impact of *HAVCR2*$^+$*VSIR*$^+$ TAM signature on overall survival (OS) of patients with cancer in TCGA datasets consisting of six pan-cancer immune landscape classes (C1, n = 2067; C2, n = 2424, C3, n = 2349; C4, n = 1142, C5, n = 387; C6, n = 180) (for more details, see fig. S2, A and B, and table S1). (**F** and **G**) Kaplan-Meier curve of patients with cancer spanning five cancer types (skin cutaneous melanoma, bladder cancer, kidney cancer, glioblastoma, and stomach adenocarcinoma), where tumors were transcriptome-profiled before anti-PD(L)1 and/or anti-CTLA4 antibody treatments. Kaplan-Meier curve shows (F) OS (n = 152) and (G) progression-free survival (PFS) (n = 129) of *HAVCR2*$^+$*VSIR*$^+$TAM signature$^{\text{HIGH}}$ versus *HAVCR2*$^+$*VSIR*$^+$TAM signature$^{\text{LOW}}$ patients (statistical autocutoff for expression; log-rank test for P value).

analyzed existing tumor transcriptomes of 11 commonly used (subcutaneous) murine models in immuno-oncology (*37*) for genetic signatures of proimmunogenic IFN-γ signaling versus MΦs (*21*, *37*). Through this, we selected the following representative tumor models: nonimmunogenic Lewis lung carcinoma (LLC) (MΦ$^{\text{HIGH}}$IFN-γ signaling$^{\text{LOW}}$) versus immunogenic MC38 (MΦ$^{\text{LOW}}$IFN-γ signaling$^{\text{HIGH}}$) (fig. S3A). In vivo analyses showed that LLC tumors indeed had a CD11b$^+$F4/80$^+$TAMs$^{\text{HIGH}}$CD4$^+$/CD8$^+$ T cells$^{\text{LOW}}$ phenotype and higher anti-inflammatory M2-like TAMs [Colony stimulating factor 1 receptor (CSF1R)$^{\text{HIGH}}$major histocompatibility complex II (MHCII)$^{\text{LOW}}$ and CD206$^{\text{HIGH}}$MHCII$^{\text{LOW}}$] compared to MC38 tumors (Fig. 3A; fig. S3, B and D; and flow cytometry gating in the Supplementary Materials). Accordingly, LLC tumors were resistant to PD1/PD-L1 blockade (Fig. 3B), whereas MC38 tumors were significantly susceptible (Fig. 3C). When we analyzed the TAMs compartment in LLC and MC38 tumors, via an unsupervised computational approach, we found TIM3$^+$VISTA$^+$CSF1R$^+$TAMs in both contexts (blue populations) with visually higher accumulation in LLC tumors (Fig. 3, D to G). The TIM3$^+$VISTA$^+$CSF1R$^+$TAMs showed tumor type–dependent heterogeneity in terms of number of clusters (Fig. 3, D and F, and fig. S3, E and F). The LLC tumors highly enriched for the immunosuppressive clusters of these TAMs, i.e., CD206$^{\text{HIGH}}$ and CD206$^{\text{HIGH}}$MHCII$^+$ (Fig. 3D). MC38 and LLC tumors primarily shared the partially activated subset, i.e., MHCII$^+$. Immunoresistant LLC tumors enriched significantly more TIM3$^+$VISTA$^+$ TAMs than MC38 tumors (Fig. 3, H and I). Confirmatively, the TIM3$^+$VISTA$^+$ TAMs in LLC tumors showed substantial expression of anti-inflammatory markers such as CSF1R and/or CD206 (Fig. 3I), and this was higher than MC38 tumors (Fig. 3, J and K). Last, above patterns were TIM3/VISTA-specific because for PD1, which was also reported on TAMs (*15*), the trend was significantly opposite (fig. S3G). Notably, while TIM3$^+$VISTA$^+$phenotype was the most proficient in TAMs, it was also recoverable from bone marrow–derived MΦs (BMDMs) (fig. S3H) or J774 murine MΦ-like cells (fig. S3I), thus emphasizing its broad origins. In conclusion, TIM3$^+$ VISTA$^+$ TAMs exhibit a cross-species enrichment in nonimmunogenic tumors.

TIM3$^+$VISTA$^+$ TAMs are hyperphagocytic with an anti-inflammatory phenotype

We wondered whether the phenotypic human-to-mouse conservation of TIM3$^+$VISTA$^+$ TAMs was also recapitulated on molecular levels. For this, we reanalyzed our previously published scRNA-seq data for LLC tumor–derived CD45$^+$ cells (Fig. 3L) (*38*). Notably, a strong *Havcr2*$^+$*Vsir*$^+$ phenotype was specific for TAMs [particularly for Imm TAM-1 subset, also showing high expression of *Ccr2*, *Mafb*, and *Csf1r* (*38*)] (Fig. 3M). As opposed to this, none of the DC subsets, other myeloid cells, CD4$^+$/CD8$^+$ T cells, B cells, or NK cells showed a proficient *Havcr2*$^+$*Vsir*$^+$ phenotype (Fig. 3M and fig. S4A). This was also confirmed via in vivo tumor immunophenotyping for TIM3$^+$VISTA$^+$ status (Fig. 3N) and TIM3$^+$ or VISTA$^+$ alone (fig. S4B). Together, this proved that TIM3$^+$VISTA$^+$ phenotype is specific for TAMs in both mouse and human tumors.

Next, we did a differential pathway enrichment analysis between *Havcr2*$^+$*Vsir*$^+$ versus *Havcr2*$^{\text{NEG}}$*Vsir*$^{\text{NEG}}$TAMs from LLC tumors. *Havcr2*$^+$*Vsir*$^+$TAMs enriched for pathways connected to anti-inflammatory activity [e.g., IL-4/transforming growth factor–β (TGFβ) production, fibrinolysis, complement activation, and vascular endothelial growth factor receptor signaling], efferocytosis (e.g., recognition of apoptotic cell), and proinflammatory signaling (e.g., Toll-like receptor or TLR signaling) (fig. S4C). For both human and mouse TIM3$^+$VISTA$^+$ TAMs, phagocytotic/efferocytotic pathways were redundantly enriched. Since heightened efferocytotic activity is crucial modulator of MΦ–cancer cell interface (*39*), we investigated this by exposing TAMs and BMDMs (MΦ) to pHrodo-labeled *Escherichia coli* particles. The TIM3$^+$VISTA$^+$ TAMs/MΦ were hyperphagocytic since they phagocytosed *E. coli* particles ~60 to 70% higher than TIM3$^{\text{LOW}}$VISTA$^{\text{LOW}}$TAMs/MΦ (Fig. 3O). Together, this confirmed cross-species conservation of molecular characteristics of TIM3$^+$VISTA$^+$ TAMs.

TIM3$^+$VISTA$^+$ TAMs blunt ICD in nonimmunogenic murine tumors

We pursued therapeutic blockade of TIM3 or VISTA via antibodies to blunt the TIM3$^+$VISTA$^+$ TAMs. Unexpectedly, both LLC (fig. S5A) and MC38 (fig. S5B) tumors were resistant to TIM3 or VISTA blockade. Even TIM3/VISTA and PD1 coblockade (*9*) either did not affect the growth of LLC tumors (fig. S5C) or did not outperform PD1 blockade for MC38 tumors (fig. S5D). Thus, despite being immunoresistant and strongly enriching TIM3$^+$VISTA$^+$ TAMs, LLC tumors were resistant to unimodal TIM3 or VISTA blockade. We wondered whether targeting other TAM-relevant pathways was more impactful than TIM3/VISTA blockade. Hence, on the basis of differentially enriched pathways between *HAVCR2*$^+$*VSIR*$^+$ versus *HAVCR2*$^{\text{NEG}}$*VSIR*$^{\text{NEG}}$TAMs (fig. S1, C and D), we tried in vivo targeting of several well-established TAM-relevant targets, i.e., signal regulatory protein α (SIRPα), CD40, complement receptor type 1 and 2 (CR1/2), FcγRII/III, IL-10, CCL2, IL-1β or TGFβ. LLC tumors were completely resistant to blockade (SIRPα, CD40, CR1/2, FcγRII/III, IL-10, CCL2, IL-1β, and TGFβ) or agonism (CD40) of these TAM-relevant targets (fig. S5E). This highlighted the extreme challenges of targeting immunoresistant tumors.

This made us wonder whether proinflammatory repolarization of TIM3$^+$VISTA$^+$ TAMs offered better therapeutic opportunities. Above scRNA-seq data had indicated the affinity of TIM3$^+$VISTA$^+$ TAMs for efferocytosis and danger signaling. ICD is a therapeutic cell death subroutine, which is well established to propagate danger signaling and create an immunogenic efferocytotic interface with myeloid cells (*40*, *41*). Hence, we pursued combinatorial treatment with a widely used ICD-inducing chemotherapy, i.e., paclitaxel (PTX) (*40*, *42*). We took along a well-established non-ICD–inducing chemotherapy as negative control, i.e., cisplatin (CDDP) (*43*). In vitro, both PTX- and CDDP-treated LLC/MC38 cancer cells underwent cell death (fig. S5, F to I) with apoptotic features (fig. S5, J and K) and passively secreted danger signals such as extracellular adenosine 5′-triphosphate (ATP) (fig. S6, A and B) or high mobility group box 1 (HMGB1) (fig. S6C). However, only PTX-treated cancer cells showed ICD-specific markers (*44*), i.e., surface heat shock protein 90 (HSP90)$^{\text{HIGH}}$CD47$^{\text{LOW}}$ (fig. S6, D and E) and surface calreticulin$^{\text{HIGH}}$CD47$^{\text{LOW}}$ (fig. S6, F and G). Ex vivo TIM3$^+$VISTA$^+$ TAMs established a more proficient efferocytotic interface with PTX-treated cancer cells (fig. S7, A and B). TIM3 or VISTA blockade significantly reduced efferocytosis of dying cancer cells by MΦs (fig. S7, C to F), thereby validating the direct proefferocytotic contribution of TIM3/VISTA.

Unexpectedly, in vivo LLC and MC38 tumors were susceptible to CDDP (Fig. 4, A and B) but resistant to PTX (Fig. 4, C and D). We specifically chose the same concentration for CDDP and PTX to allow us to compare both chemotherapies with each other. In LLC tumors, TIM3 or VISTA blockade synergized with only PTX to cause

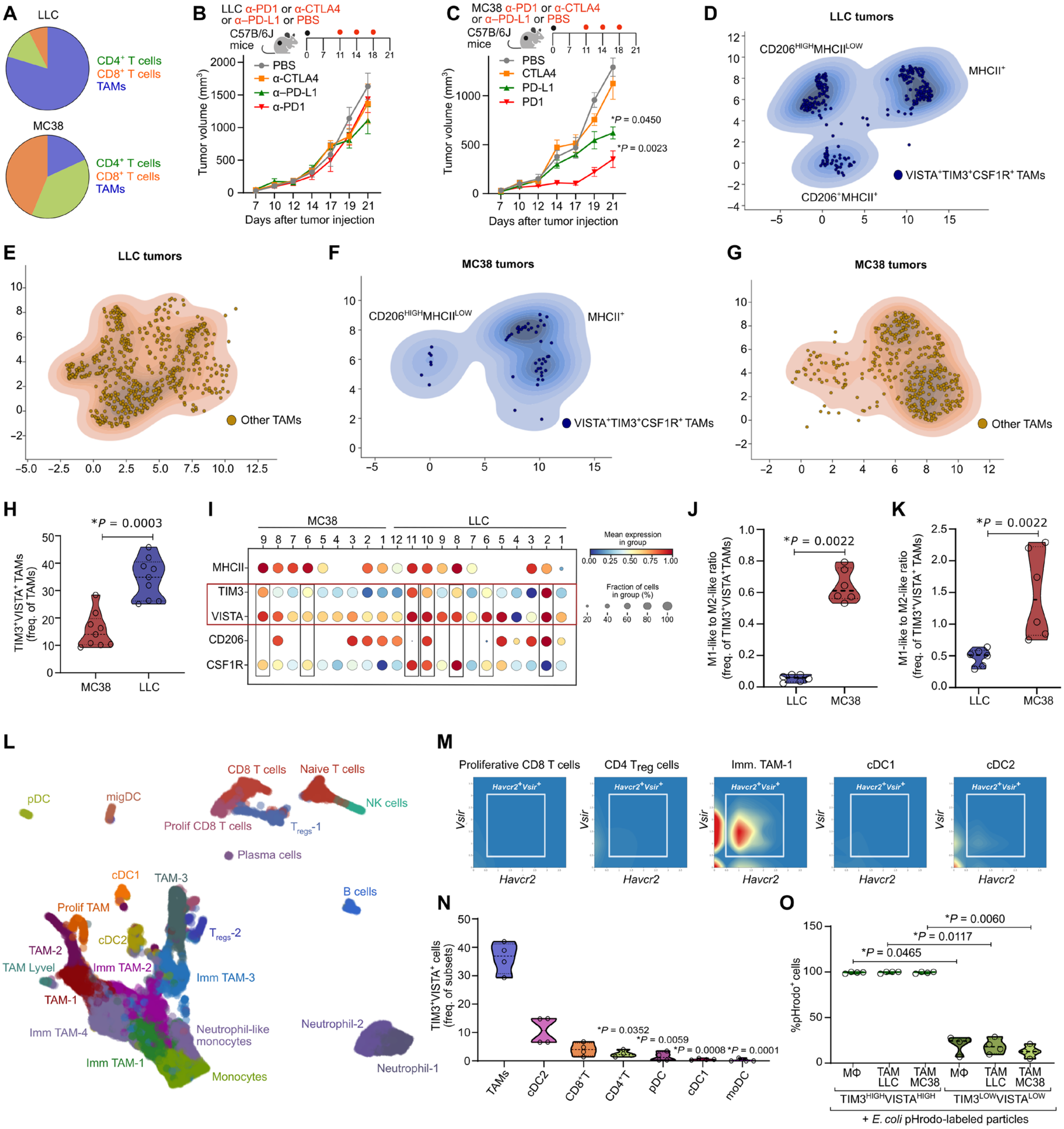

Fig. 3. TIM3$^+$VISTA$^+$ TAMs have an anti-inflammatory phenotype and dominantly enrich in an immunoresistant murine tumor. (**A**) Basal immunophenotyping of LLC and MC38 tumors, showing percentages of CD8$^+$ T cells, CD4$^+$ T cells, and TAMs ($n = 5$). See fig. S3B for the violin plots and statistics. (**B** and **C**) Tumor volume curve of (B) LLC and (C) MC38 tumor–bearing mice treated with anti-PD1/PD-L1/CTLA4 antibody or phosphate-buffered saline (PBS) [$n = 4$; Kruskal-Wallis test corrected for false discovery rate (FDR)]. (**D** to **G**) KDE plots showing TAM populations in LLC and MC38 tumors from flow cytometry data of CD45$^+$ cell fraction obtained from LLC and MC38 tumors. KDE plots were made on the basis of the Uniform Manifold Approximation and Projections (UMAPs) shown in fig. S3 (E and F). (**H**) Percentage of TIM3$^+$VISTA$^+$ TAMs in LLC and MC38 tumors ($n = 9$; Mann-Whitney test). (**I**) Different markers used in Fig. 2 (D to G) for LLC and MC38 tumor samples. Size of dots represents fraction of cells and color intensity represents mean expression levels in each group. (**J** and **K**) CD45$^+$ cell fraction from LLC and MC38 tumors. (J) Ratio of M1-like (MHCII^{HIGH}CSF1R^{LOW}) TAMs to M2-like (CSF1R^{HIGH}MHCII^{LOW}) TAMs and (K) ratio of M1-like (MHCII^{HIGH}CD206^{LOW}) TAMs to M2-like (CD206^{HIGH}MHCII^{LOW}) TAMs of TIM3$^+$VISTA$^+$ TAMs ($n = 6$; Mann-Whitney test). (**L**) UMAP of scRNA-seq data from LLC tumors. (**M**) scRNA-seq LLC tumor tissue dataset, showing *Vsir* and *Havcr2* in different immune cell subsets. (**N**) Percentage of TIM3$^+$VISTA$^+$ on CD8$^+$ and CD4$^+$ T cells, TAMs, and DCs—conventional DC 1 (cDC1) and cDC2, monocytic DC (moDC), and plasmacytoid DC (pDC)—in LLC tumors ($n = 4$; Kruskal-Wallis test corrected for FDR, comparison to TAMs). (**O**) pHrodo Green$^+$ TIM3$^+$VISTA$^+$ CD11b$^+$ F4/80$^+$ or TIM3$^-$VISTA$^-$ CD11b$^+$ F4/80$^+$ in cocultures of BMDMs or TAMs from LLC or MC38 tumors, cocultured with pHrodo labeled *E. coli* bioparticles ($n = 4$; Kruskal-Wallis test corrected for FDR). *N* number represents number of biological repeats or number of independent animals used.

significant reduction in tumor growth (Fig. 4, A and C). This synergism was absent in MC38 tumors (Fig. 4, B and D). In both models, TIM3 or VISTA blockade was not beneficial in combination with CDDP (Fig. 4, A and B).

Notably, combination of PTX with TIM3/VISTA blockade significantly reduced the TIM3$^+$VISTA$^+$CSF1R$^+$TAMs (Fig. 4E). This combination skewed these TAMs toward a more proinflammatory M1-like (MHCII^{HIGH}CSF1R^{LOW}) phenotype as compared to anti-inflammatory M2-like (MHCII^{LOW}CSF1R^{HIGH}) (Fig. 4F). Above switch from anti- to proinflammatory phenotype was TIM3/VISTA-driven because in LLC-MΦ cocultures in vitro, TIM3 or VISTA blockade together with PTX-treated LLC cells caused increased enrichment of activated MHCII^{HIGH}MΦs (fig. S8, A and B). Notably, the triple combination of PTX treatment with TIM3 and VISTA coblockade was not significantly different from doublet combinations (fig. S8C). Thus, TIM3/VISTA blockade synergizes with ICD-inducing chemotherapy to repolarize TIM3$^+$VISTA$^+$ TAMs toward proinflammatory phenotype, which associated with blunting of tumors.

Antitumor synergism between TIM3/VISTA blockade and ICD depends on TAMs

Blunted LLC tumors did not experience increased infiltration of CD4$^+$/CD8$^+$ T cells (Fig. 4G and fig. S9A). An extended phenotyping of T cells further highlighted that regressing LLC tumors failed to enrich any of the typical antitumor T cell subsets such as proliferating Ki67$^+$CD8$^+$/CD4$^+$ T cells (fig. S9, B and C), effector memory CD127$^+$CD62L$^-$CD8$^+$/CD4$^+$ T cells (fig. S9, D and E), effector IFN-γ^+ (fig. S9, F and G) or IL-2$^+$ (fig. S9, H and I) CD8$^+$/CD4$^+$ T cells, or cytotoxic CD107a$^+$CD8$^+$ T cells (fig. S9J). Similarly, the regressing LLC tumors did not enrich any of the different DC subsets (fig. S10, A to C) or their matured/activated states (fig. S10, D to F). This indicated that the synergism of TIM3/VISTA blockade with PTX primarily associated with activation of TAMs.

To validate this, we depleted MΦs via clodronate liposomes and CD8$^+$ T cells via anti-CD8 antibodies (*45*). Clodronate liposomes were applied at a titrated dose that depleted TAMs and splenic MΦs (fig. S11, A and B) but did not affect DCs (fig. S11, A and B). Clodronate liposome–based MΦ depletion already substantially affected tumor growth compared to the phosphate-buffered saline (PBS) control (Fig. 4H). MΦ depletion completely reshaped the chemotherapy susceptibility of LLC tumors. PTX treatment by itself reduced the tumor growth now (Fig. 4H), such that the synergism of PTX with TIM3 or VISTA blockade disappeared (Fig. 4H). To further investigate this direct modulation of PTX resistance, we sorted TIM3$^+$VISTA$^+$ TAMs and TIM3^{NEG}VISTA^{NEG}TAMs from LLC tumors. These TAMs were cocultured with untreated (UT) LLC cancer cells, followed by PTX treatment. Presence of TIM3$^+$VISTA$^+$ TAMs mediated resistance to PTX, since under, specifically, this condition, we did not observe LLC cell death (fig. S11C). In contrast, the depletion of CD8$^+$ T cells (fig. S11, D and E) did not significantly disrupt synergism of PTX and TIM3/VISTA blockade (Fig. 4I).

Next, we wished to molecularly confirm these patterns. Hence, we used an antibody array to analyze protein levels of multiple cytokines/chemokines or other immune factors (*43*) in CD45$^+$ cells from LLC tumors. Under all conditions, there was no enrichment of typically adaptive immune cytokines/factors (fig. S12A). However, a very specific enrichment of cytokines/chemokines/factors relevant for myeloid cells or TAMs was seen in UT and PTX-treated LLC tumors (Fig. 4J). These were almost completely depleted in LLC tumors suppressed by treatment with PTX and TIM3/VISTA blockade (Fig. 4J). Thus, the therapeutic synergism of TIM3/VISTA blockade and ICD-inducing chemotherapy is completely dependent on only TAMs.

TIM3$^+$VISTA$^+$ TAMs autonomously enforce anticancer cytotoxicity via TRAIL signaling

Next, we were curious about the exact molecular pathway used by TIM3$^+$VISTA$^+$ TAMs to suppress LLC tumors in absence of antitumor T cells. LLC tumors suppressed by our combinatorial regimen showed a significant increase in apoptosis (marked by cleaved caspase 9) (Fig. 4K). In ex vivo cocultures of LLC tumor–derived TAMs and LLC cells, blockade of TIM3 or VISTA potentiated proapoptotic stress in LLCs (fig. S12B). All this suggested that, perhaps, TAMs were directly killing cancer cells.

To validate whether, and how, TAMs were directly killing the cancer cells, we isolated TAMs from LLC tumors that were either treated with PBS or PTX and blocked major MΦ-associated cytotoxicity pathways (*16*, *46*) in presence of UT LLC cancer cells ex vivo (Fig. 4L). Specifically, we blocked the respiratory burst through various agents: apocynin (blocks nicotinamide adenine dinucleotide phosphate oxidase complex–based H_2O_2 production) (*46*), catalase (degrades H_2O_2) (*47*), and N^G-monomethyl-L-arginine, monoacetate salt (L-NMMA) (blocks nitric oxide synthase–based NO production) (*48*, *49*); and we blocked various effectors of the extrinsic cell death pathway via antibodies, i.e., TNF (*49*), TRAIL (*16*), and Fas ligand (FasL) (*50*). These cocultures confirmed that PTX-treated tumor-derived TAMs, in presence of TIM3/VISTA blockade, caused significant LLC cancer cell death (Fig. 4L). Of all the different pathway ablations, this TAM-driven cancer cell death was specifically disrupted only by the blockade of TRAIL (Fig. 4L). This suggested that proinflammatory activation of TIM3$^+$VISTA$^+$ TAMs created TAM-driven anticancer cytotoxicity via TRAIL signaling.

TAM-specific genetic ablation of TIM3 and VISTA synergizes with ICD-inducing chemotherapy to blunt nonimmunogenic tumors

Since TIM3$^+$VISTA$^+$ TAMs were connected with CSF1R$^+$TAMs (Fig. 3I), we wondered whether the synergism of PTX with TIM3/VISTA blockade was extendable to antibody-based CSF1R blockade. However, in vivo analyses did not show substantial tumor reduction upon combining PTX with CSF1R blockade (fig. S12C). Notably, while the CSF1R blockade significantly depleted CSF1R$^+$TAMs (fig. S12D), it failed to deplete TIM3$^+$VISTA$^+$CSF1R$^+$TAMs (fig. S12E). Inefficiency of CSF1R blockade in depleting particular TAM subsets in vivo has been reported previously (*36*). These discrepant results demanded a stronger TIM3/VISTA-specific genetic ablation approach directed toward CSF1R$^+$TAMs.

To accomplish this specifically in CSF1R$^+$MΦs in vivo, we first used lentiviral particles simultaneously expressing guide RNAs (gRNAs) against both *Havcr2* and *Vsir* to transduce hematopoietic stem/progenitor cells (HSPCs) from *Csf1r:Cre-ERT/R26:LSL-Cas9* mice (donor mice; CD90.1 congenic strain), carrying a (conditional) tamoxifen-inducible *Cas9* in CSF1R$^+$ cells (Fig. 4M). In this way, *Havcr2* (fig. S12F) and *Vsir* (fig. S12G) were simultaneously knocked down by at least 60% in the MΦs. Transduced HSPCs were transplanted into lethally irradiated recipients to create recipient mice with tamoxifen-inducible *Havcr2*$^-$*Vsir*$^-$ phenotype in CSF1R$^+$MΦs (i.e., *Havcr2*$^-$*Vsir*$^-$ΔMΦ phenotype) (Fig. 4M). Control mice were set

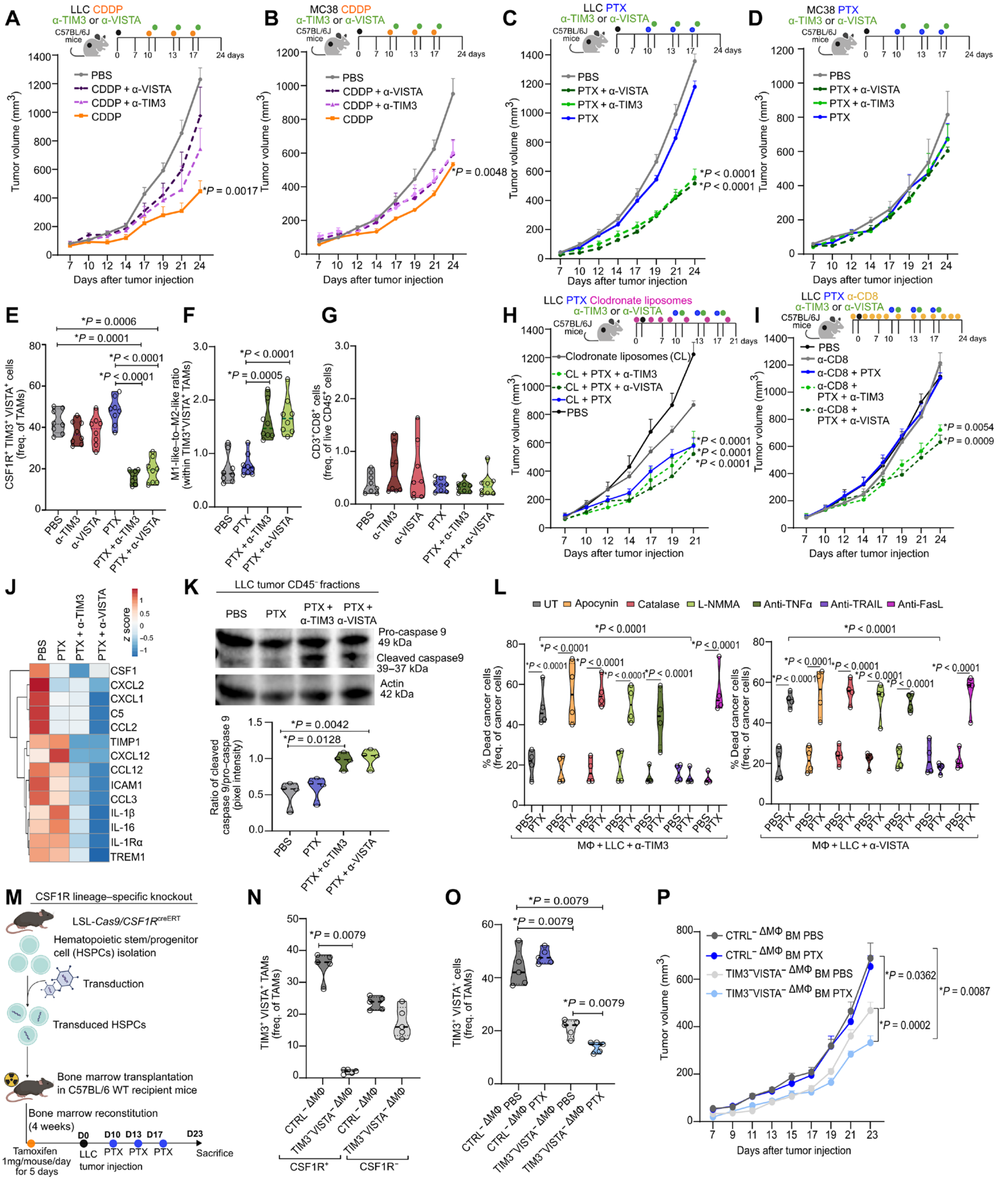

Fig. 4. Antitumor synergism between TIM3/VISTA blockade and ICD depends on MΦs. (**A** and **B**) Tumor volume curve of (A) LLC tumors and (B) MC38 tumors treated with CDDP or PBS with anti-TIM3/VISTA antibody (LLC, $n = 8$; MC38, $n = 4$; Kruskal-Wallis test corrected for FDR). (**C** and **D**) Tumor volume curve of (C) LLC tumors and (D) MC38 tumors treated with PTX or PBS with anti-TIM3/VISTA antibody (LLC, $n = 10$; MC38, $n = 4$; Kruskal-Wallis test corrected for FDR). (**E** to **G**) CD45$^+$ cell fraction obtained from (C). (E) Percentage of TIM3$^+$VISTA$^+$ TAMs ($n = 8$; Kruskal-Wallis test corrected for FDR). (F) Ratio of M1-like (MHCII^{HIGH}CSF1R^{LOW}) TAMs to M2-like (CSF1R^{HIGH}MHCII^{LOW}) TAMs ($n = 8$; Kruskal-Wallis test corrected for FDR). (G) Percentage of CD8$^+$ T cells ($n = 8$; Kruskal-Wallis test corrected for FDR). (**H** and **I**) Tumor volume curve of LLC tumors treated with PTX or PBS and/or anti-TIM3/VISTA antibody (H) combined with clodronate liposomes ($n = 9$; Kruskal-Wallis test corrected for FDR, comparison to PBS) and (I) combined with anti-CD8 antibody ($n = 8$; Kruskal-Wallis test corrected for FDR, comparison to PBS). (**J** and **K**) Lysate from CD45$^-$ cell fraction obtained from (C). (J) Protein levels of different analytes. Incalculable values are depicted as gray ($n = 4$). (K) Pro–caspase 9, cleaved caspase 9, and actin Western blot. Ratio of quantification of pixel intensity is represented in a violin plot ($n = 4$; Kruskal-Wallis test corrected for FDR.) (**L**) Percentages of cancer cell death after coincubation with TAMs with different inhibitors [$n = 4$; two-way analysis of variance (ANOVA) corrected for FDR]. (**M**) Overview of a CRISPR-Cas9–mediated *Vsir* and *Havcr2* knockout in CSF1R$^+$ cells (MΦs) (created with BioRender.com). WT, wild-type. (**N** to **P**) LLC tumor–bearing TIM3$^-$VISTA$^-$ MΦ or control knockout MΦ mice, treated with PTX or PBS. (N) Percentages of CSF1R$^+$ and CSF1R$^-$ TIM3$^+$VISTA$^+$ TAMs ($n = 5$; Kruskal-Wallis test corrected for FDR). (O) Percentages of TIM3$^+$VISTA$^+$ TAMs ($n = 5$; Kruskal-Wallis test corrected for FDR). (P) Tumor volume curve (control knockout PTX, $n = 8$; others, $n = 6$; Kruskal-Wallis test corrected for FDR).

up with nontargeting control gRNA. Both these mice groups were either left UT (PBS) or treated with PTX (Fig. 4M). Confirmatively, all these mice had similar levels of circulating CD90.1$^+$ (donor) immune cells (fig. S12H), and TIM3$^+$VISTA$^+$CSF1R$^+$ MΦs were almost completely depleted in the TIM3$^-$VISTA$^{-\Delta M\Phi}$ mice (Fig. 4N), highlighting the knockout efficiency of the model. In addition, there was a reduction of >60% in enrichment of TIM3$^+$VISTA$^+$ TAMs (Fig. 4O), and this reduction in TIM3$^+$VISTA$^+$ phenotype was specific for TAMs (fig. S12I) rather than tumor-derived DCs or CD4$^+$/CD8$^+$ T cells (fig. S12, J to L), highlighting the knockout specificity of the used model.

Using these mice, we observed that *Havcr2*$^-$*Vsir*$^-$ MΦs already resulted in a modest, albeit significant, reduction in LLC tumor growth compared to control mice (Fig. 4P). However, the most significant reduction of LLC tumor growth was achieved upon PTX treatment, thereby confirming synergism between this chemotherapy and MΦ-specific *Havcr2*/*Vsir* ablation (Fig. 4P). Accordingly, PTX treatment and MΦ-specific *Havcr2*/*Vsir* ablation resulted in the highest enrichment of proinflammatory MHCII^{HIGH}CSF1R^{LOW}TAMs (fig. S12M). There was no increase in infiltration of CD8$^+$/CD4$^+$ T cells or IFN-γ$^+$CD8$^+$ T cells (fig. S12, N to P). This confirmed that TAM-specific TIM3/VISTA blockade is necessary for maximal tumor blunting by ICD-inducing chemotherapy.

Low tumoral antigenicity drives IL-4–driven accumulation of TIM3$^+$VISTA$^+$ TAMs

It was essential to uncover the mechanism behind preferential enrichment of TIM3$^+$VISTA$^+$ TAMs in LLC tumors. Hence, we pursued differential gene expression (DGE) analysis of bulk transcriptomes of LLC versus MC38 tumors (fig. S3A). LLC tumors enriched for immunosuppressive genes linked to prostaglandin E2 (PGE2) signaling (*Ptgs1* and *Cox5a*), IL-1 signaling (*Il18rap* and *Il1r1*), TGFβ signaling (*Tgfbr3*), anti-inflammatory TAMs (*Mrc1*, *Ccr2*, *Cd33*, and *Gas2*), or IL-4/IL-13 pathway (*Il4ra*) (Fig. 5A). Contrastingly, genes relevant for immunogenic pathways including IFN-stimulated gene (ISG) response (*Rsad2*, *Oasla*, *Oas2*, *Oasl1/2*, *Mx2*, *Stat1/2*, *Ifi44*, and *Cxcl9*), cytotoxic lymphocyte activity (*Gzmf*, *Gzmd*, and *Gzmb*), and tumor-relevant antigens (*Magea10* and *Magea1*) were enriched in MC38 tumors (Fig. 5A).

We wondered whether one or more of the promyeloid factors that featured prominently in LLC tumors caused accumulation of TIM3$^+$VISTA$^+$ TAMs. Hence, we tested the ability of above LLC tumor–specific cytokines/factors to differentiate murine BMDMs. We incubated these MΦs with TGFβ, PGE2, IL-1β, IL-18, IL-4, IL-13, and an anti-inflammatory differentiation cocktail for MΦs (IL-4 + IL-13), in vitro (Fig. 5B). The most potent inducer of TIM3$^+$VISTA$^+$phenotype was the cytokine cocktail, primarily led by IL-4 (Fig. 5B). This aligned with the strong anti-inflammatory (fig. S1, C and D) and IL-4 signaling character (fig. S4C) of *Havcr2*$^+$*Vsir*$^+$TAMs in LLC tumors. Therefore, we also looked at the in vivo enrichment of IL-4 or IL-13 relative to total TAMs (to account for the difference in TAMs between LLC and MC38 tumors). We observed that TAMs in LLC tumors were significantly more exposed to IL-4 (Fig. 5C) or IL-13 (Fig. 5D) compared to the MC38 tumors. Since IL-4 was the most potent inducer of TIM3$^+$VISTA$^+$phenotype, we neutralized IL-4 via a depleting antibody in vivo, in both MC38 and LLC tumors (fig. S13, A and B). MC38 tumors were not affected upon neutralizing IL-4. In contrast, growth of LLC tumors were significantly reduced by neutralizing IL-4 (fig. S13B), such that IL-4 neutralization also significantly reduced the amount of TIM3$^+$VISTA$^+$ TAMs (fig. S13C).

Tumoral IL-4 is a sign of type 2 anti-inflammatory responses (*16*, *51*). These responses dominate immunoresistant tumors; however, their dominance is more limited in antigenic/immunogenic tumors (*52*). Since MC38 tumors showed higher antigenicity/immunogenicity than LLC tumors, we wondered whether the lack of strong antigens within LLC tumors ultimately facilitated IL-4 enrichment, thereby sustaining TIM3$^+$VISTA$^+$ TAMs. To ameliorate this, we genetically manipulated the LLC cells to express the well-established model antigen, ovalbumin (OVA). Notably, simply expressing OVA-antigen in LLCs converted the resulting in vivo tumor milieu into a more MC38-like, i.e., TAMs in LLC-OVA tumors were exposed to lower IL-4/IL-13 levels (Fig. 5, E and F), and the immune landscape was more immunogenic (TAMs^{LOW}CD4$^+$/CD8$^+$ T cells^{HIGH}) (Fig. 5G and fig. S13D). Accordingly, LLC-OVA tumors enriched significantly less TIM3$^+$VISTA$^+$ TAMs (Fig. 5H) and even those that they did enrich had more proinflammatory orientation (CSF1R^{LOW}MHCII^{HIGH}) (fig. S13E). Accordingly, the therapeutic synergism between PTX and TIM3/VISTA blockade disappeared in LLC-OVA tumors (Fig. 5I). This established that low antigenic tumors facilitate an IL-4–driven exaggerated accumulation of TIM3$^+$VISTA$^+$ TAMs.

TIM3 and VISTA inhibit TAM-intrinsic ISG responses, thereby blunting ICD

The mechanistic basis behind synergism of ICD-inducing PTX with TIM3/VISTA blockade was still unclear. However, one observation in above DGE analyses provided us with a clue. While the ISG response was enriched in MC38 tumors, a gene coding for type I IFN receptor (*Ifnar1*) was enriched in LLC tumors, indicating a misalignment between type I IFN sensing and downstream ISG response. This needed attention because ICD relies on type I IFNs to exert antitumor efficacy (*53*).

Accordingly, only LLC cells undergoing ICD via PTX autonomously secreted type I IFN (IFN-β) (Fig. 5J). This was not significantly potentiated upon cocultures with MΦs and TIM3/VISTA blockade, thus emphasizing LLCs as primary IFN-β producers (Fig. 5J). Next, we checked levels of downstream ISGs (*Rsad2*, *Mx1*, *Irf7*, and *Cxcl10*), and, unexpectedly, no clear ISG response was detected when PTX-treated LLCs were cocultured with MΦs (Fig. 5K). This implied that IFN-β failed to activate ISG response. TIM3 or VISTA blockade successfully reinstated the ISG response (Fig. 5K). In a coculture setting, it is hard to confirm whether ISG response is intrinsic to cancer cells or MΦs. To overcome this, we repeated above analyses with J774 MΦs expressing a luciferase-based genetic reporter linked to downstream ISG response (*21*). With this, we successfully reproduced the above patterns (Fig. 5, L and M) and confirmed that TIM3/VISTA blockade–driven ISG response was intrinsic to MΦs.

ICD-associated type I IFN production is driven by dying cell-derived extracellular nucleic acids (*43*, *53*). To verify this, we repeated above experiments while degrading nucleic acids via deoxyribonuclease (DNase)/ribonuclease (RNase) (*43*). Degradation of extracellular nucleic acids strongly ablated production of IFN-β (Fig. 5, N and O) and MΦ-intrinsic ISG responses (Fig. 5, P and Q). Thus, although ICD triggered autocrine type I IFNs via sensing of extracellular nucleic acids, the paracrine ISG response in interacting MΦs was blunted by TIM3/VISTA signaling.

This suggested that TIM3/VISTA blockade synergized with PTX because it reestablished IFN-β–induced ISGs in TIM3$^+$VISTA$^+$ TAMs. Since host type I IFN receptors would be the key to this, we pursued in vivo validation with *Ifnar1*$^{-/-}$mice. Therapeutic synergism between

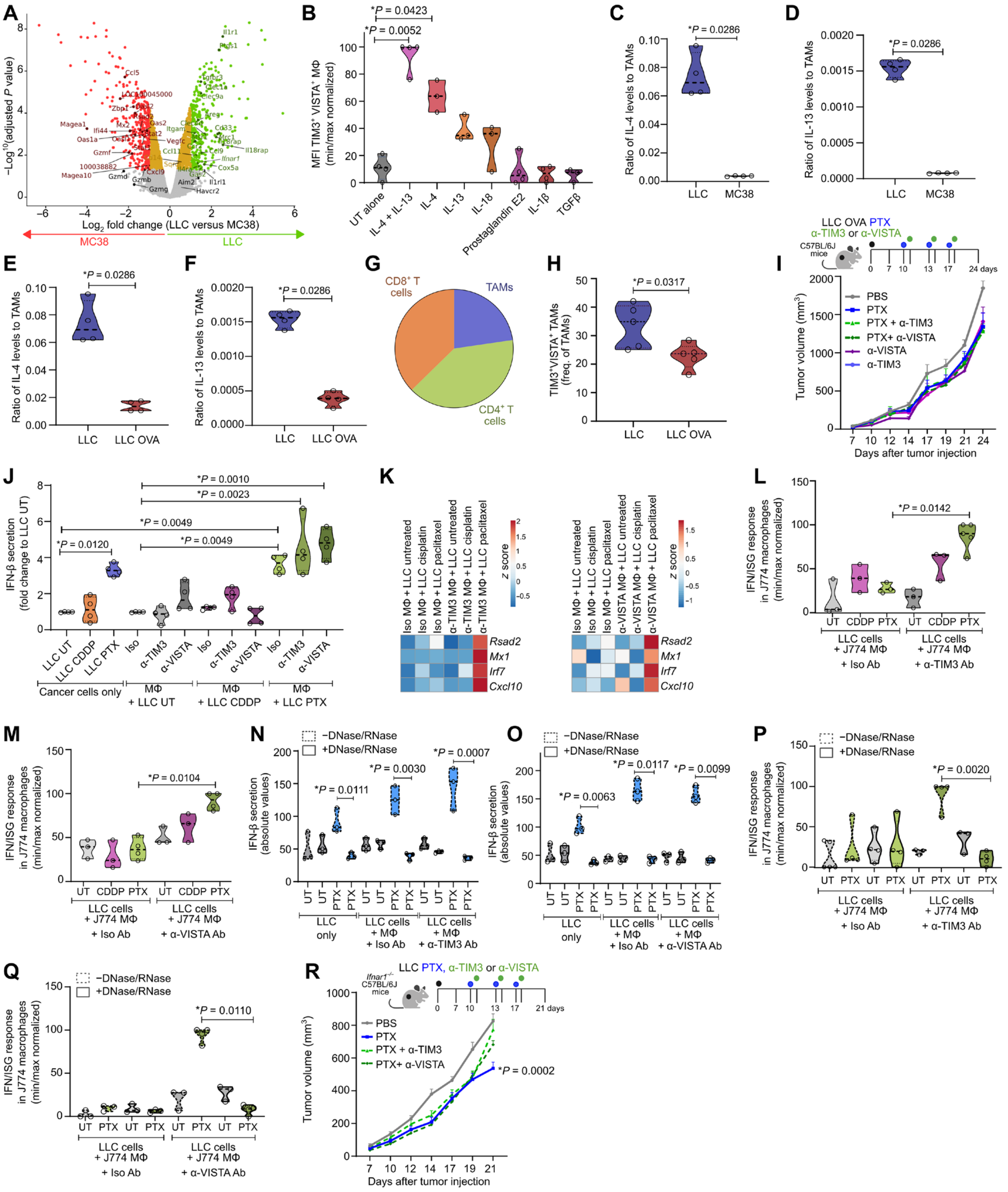

Fig. 5. TIM3 and VISTA inhibit TAM-intrinsic ISG responses, thereby blunting ICD. (**A**) Volcano plot of gene expression alterations between MC38 (red) and LLC tumors (green). (**B**) Mean fluorescence intensity (MFI) of TIM3 on VISTA$^+$ BMDMs (MΦ) stimulated with different cytokines (IL-4/IL-13/IL-18, $n = 3$; others, $n = 4$; Kruskal-Wallis test corrected for FDR). (**C** to **F**) IL-4 and IL-13 secretion in tumor lysate. Ratio of absolute values with blank was taken and ratio to total TAMs. (C and D) IL-4 (C) and IL-13 (D) production in LLC and MC38 tumors ($n = 4$; Mann-Whitney test). (E and F) IL-4 (E) and IL-13 (F) production in LLC and LLC-OVA tumors ($n = 4$; Mann-Whitney test). (**G**) Percentages of CD8$^+$ T cells, CD4$^+$ T cells, and TAMs ($n = 4$). See fig. S13D for the violin plot and statistics. (**H**) Percentage of TIM3$^+$VISTA$^+$CSF1R$^+$ TAMs in LLC and LLC-OVA tumors ($n = 5$, Mann-Whitney test). (**I**) Tumor volume curves of LLC-OVA tumors ($n = 4$; Kruskal-Wallis test corrected for FDR). (**J**) IFN-β secretion of LLC cancer cells alone and their cocultures with BMDMs, with or without blockade with indicated antibodies (Abs) ($n = 4$; Kruskal-Wallis test corrected for FDR). (**K**) Quantitative polymerase chain reaction (qPCR) of ISG expression ($n = 3$). (**L** and **M**) IFN/ISG response in J774 MΦs with blockade of isotype or (L) anti-TIM3 and (M) anti-VISTA antibody and their cocultures with LLC [(M) PTX, $n = 4$; others, $n = 3$; Kruskal-Wallis test corrected for FDR]. (**N** to **Q**) LLC alone and their cocultures with MΦ with blockade of indicated antibodies. (N and O) IFN-β secretion in (N) MΦ blocked with isotype/anti-TIM3 antibody or (O) isotype/anti-VISTA antibody ($n = 3$; Kruskal-Wallis test). (P and Q) IFN/ISG response in J774 MΦs (P) blocked with isotype/anti-TIM3 antibody or (Q) isotype/anti-VISTA antibody [TIM3 LLC untreated (UT), $n = 3$; others, $n = 4$; VISTA LLC PTX, $n = 4$; others, $n = 3$; Kruskal-Wallis test corrected for FDR]. (**R**) Tumor volume curves of LLC tumors in *ifnar1*$^{-/-}$ mice ($n = 8$; Kruskal-Wallis test corrected for FDR).

PTX and TIM3/VISTA blockade was completely lost in *Ifnar1*$^{-/-}$mice (Fig. 5R). Accordingly, this combination failed to proinflammatorily activate TIM3^{+}VISTA^{+} TAMs (fig. S13F). Thus, TIM3/VISTA signaling blunts MΦ-associated ISGs, thereby disrupting ICD-inducing chemotherapy's ability to initiate type I IFN–driven antitumor immunity.

Cancer cell–associated HMGB1 and VISTA engage TIM3 and VISTA on TAM to suppress ISGs

TIM3- and VISTA-based blunting of macrophagic ISGs cannot function without ligand-based engagement of TIM3/VISTA by cancer cells. Compared to UT LLC cells, LLC cells treated with PTX proficiently exposed multiple ligands for both TIM3, i.e., surface Ceacam1 (Fig. 6A), surface Galectin-9 (Fig. 6B), and extracellular HMGB1 (Fig. 6C) (*54*), as well as VISTA, i.e., surface P-selectin glycoprotein ligand 1 (PSGL1) (Fig. 6D) and surface VISTA (Fig. 6E) (*55*). Notably, VISTA has an exceptional receptor system, i.e., VISTA on MΦs engages in homophilic intermolecular interactions with VISTA on target cells (such as cancer cells) (*56*). To understand which of these ligands was responsible for engaging TIM3/VISTA on MΦs to blunt ISGs, we first used CRISPR-Cas9 to individually knockout the genes encoding for each of these ligands (fig. S13, G to K). Next, we treated these cells with PTX and cocultured them with J774 MΦs expressing the ISG reporter system. This revealed that only *Hmgb1*$^{-/-}$ LLCs (Fig. 6F) or *Vsir*$^{-/-}$ LLCs (Fig. 6G) successfully disrupted the J774 MΦ-intrinsic ISGs facilitated by the TIM3 or VISTA blockade, respectively. This suggested that TIM3/VISTA

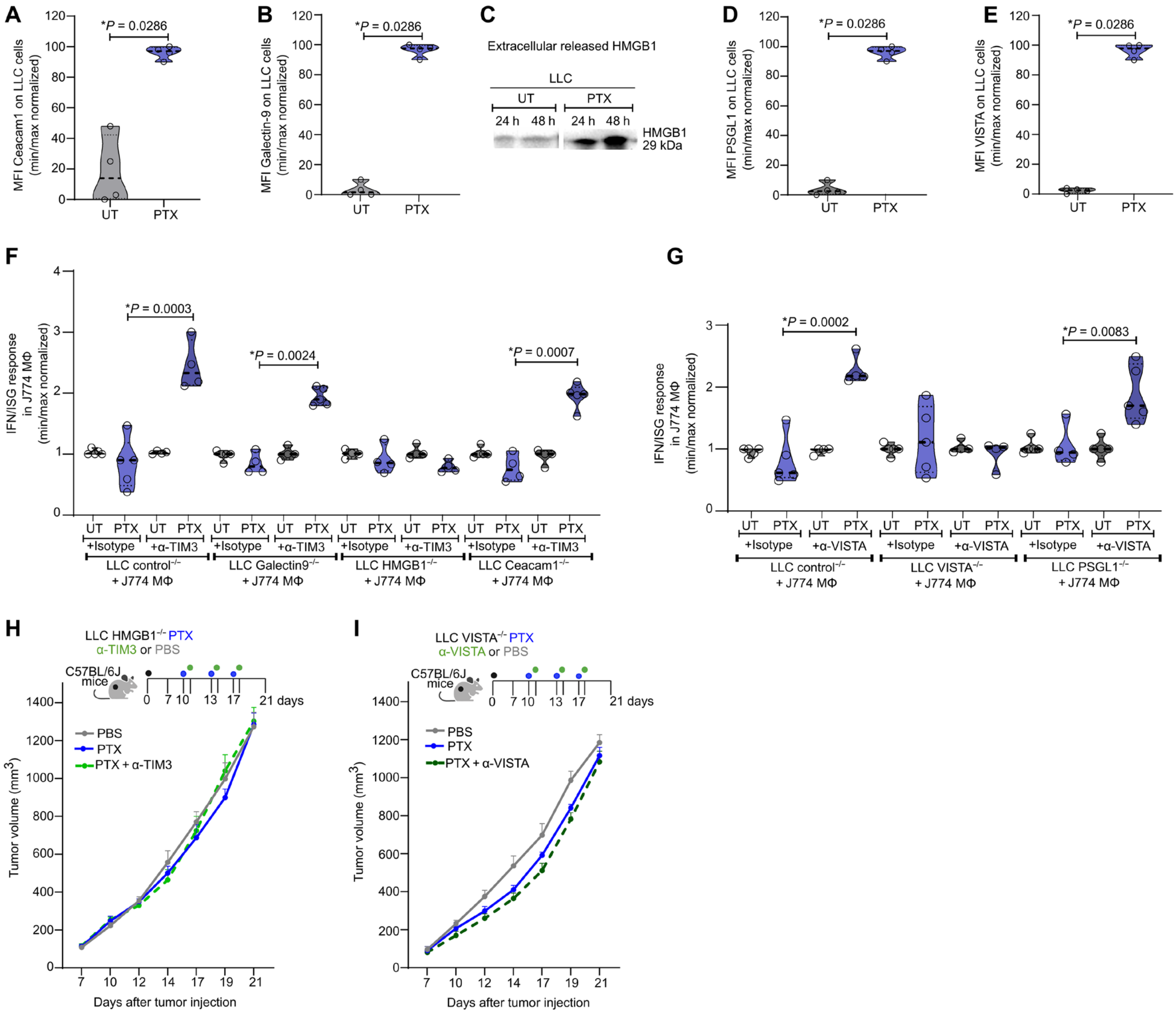

Fig. 6. Cancer cell–associated HMGB1 and VISTA engage TIM3 and VISTA on MΦs to suppress ISG responses. (**A** and **B**) MFI of (A) Ceacam1 and (B) Galectin-9 on LLC cells UT or treated for 48 hours with 100 μM PTX ($n = 4$; Mann-Whitney test). (**C**) Western blot showing extracellular released HMGB1 in LLC UT or treated for 48 hours with PTX supernatant. (**D** and **E**) MFI of (D) PSGL1 and (E) VISTA on LLC cells UT or treated for 48 hours with PTX ($n = 4$; Mann-Whitney test). (**F** and **G**) IFN/ISG response in J774 reporter MΦs with blockade with isotype antibodies or (F) anti-TIM3 antibody and their cocultures with CRISPR-Cas knockout LLC cancer cells for Adeno-associated virus serotype 1 (AAV1) empty (control), *LGALS9* (Galectin-9), *HMGB1* (HMGB1), and *CEACAM1* (Ceacam1), UT or treated with either PTX and (G) anti-VISTA antibody and their cocultures with CRISPR-Cas knockout LLC cancer cells for AAV1 empty (control), *VSIR* (VISTA), and *SELPLG* (PSGL1), UT or treated with either PTX. Values are fold-changed to UT ($n = 4$; Kruskal-Wallis test corrected for FDR). (**H**) Tumor volume curves of LLC *HMGB1*$^{-/-}$ tumors treated with PTX or PBS and/or combination with anti-TIM3 antibody ($n = 8$; Kruskal-Wallis test corrected for FDR). (**I**) Tumor volume curves of LLC *VSIR*$^{-/-}$ tumors treated with PTX or PBS and/or combination with anti-VISTA antibody ($n = 8$; Kruskal-Wallis test corrected for FDR). *N* number represents the number of biological repeats or number of independent animals used.

blockade synergized with PTX because of cancer cell–associated HMGB1/VISTA. To validate this, we pursued in vivo experiments with *Hmgb1*$^{-/-}$ or *Vsir*$^{-/-}$ LLCs. The synergism between PTX and TIM3/VISTA blockade was ablated in both *Hmgb1*$^{-/-}$ (Fig. 6H) and *Vsir*$^{-/-}$ (Fig. 6I) LLC tumors. Thus, dying cancer cells exposed HMGB1 and VISTA that engaged TIM3 and VISTA on MΦs to blunt latter's ISG responses.

Targeting TIM3$^+$VISTA$^+$ TAM impedes tumor growth in immunoresistant and neoantigen^{LOW} melanoma

It was necessary to validate above (major) features underlying TIM3$^+$VISTA$^+$ TAM enrichment and their immunotherapeutic targeting in physiologically superior orthotopic-like tumor models. Hence, we pursued validation with three subcutaneous melanoma models, i.e., *Braf*^{V600E}*Cdkn2a*$^{-/-}$*Pten*$^{-/-}$YUMM1.7 (neoantigen^{LOW}), YUMM1.7 expressing the OVA-antigen, and neoantigen^{HIGH}YUMMER1.7 (*57*, *58*).

In line with these antigenicity trends, YUMM1.7 melanoma showed a stronger TAMs^{HIGH}CD4$^+$/CD8$^+$ T cells^{LOW} phenotype (Fig. 7A and fig. S14A) than YUMM1.7-OVA (Fig. 7B and fig. S14B) or YUMMER1.7 (Fig. 7C and fig. S14C) melanomas in vivo. Confirmatively, YUMM1.7 melanomas harbored much higher TIM3$^+$VISTA$^+$CSF1R$^+$TAMs (Fig. 7D) and higher IL-4/IL-13 exposure toward TAMs (fig. S14, D and E) than YUMM1.7-OVA or YUMMER1.7 melanomas. No differences in TIM3 and VISTA expression on the level of CD8$^+$ T cells were observed between the models (fig. S14, F to H). Together, these distinct immune landscapes predicted that YUMM1.7 melanoma are resistant to PD1 blockade (Fig. 7E), whereas YUMM1.7-OVA (Fig. 7F) and YUMMER1.7 (Fig. 7G) melanomas were significantly susceptible.

Next, therapeutic testing confirmed that, while all melanoma models were resistant to PTX monotherapy, the combination of PTX and TIM3/VISTA blockade synergized to significantly blunt the growth of only immunoresistant melanoma YUMM1.7 (Fig. 7H) but not immunosusceptible counterparts YUMM1.7-OVA (Fig. 7I) or YUMMER1.7 (Fig. 7J). Above therapeutic synergism was accompanied by significant reduction in TIM3$^+$VISTA$^+$ TAMs only in YUMM1.7 melanoma (Fig. 7, K to M). Last, for CD8$^+$ T cells, we observed no statistically significant differences across all three melanoma models (Fig. 7, N to P). Together, we preclinically validated a generalizable association of TIM3$^+$VISTA$^+$ TAMs with immunoresistant or low neoantigenic tumors and the ability of ICD-inducing therapy and TIM3/VISTA blockade to specifically overcome these tumors (Fig. 8).

DISCUSSION

We characterized a human-to-mouse conserved, TAM subset, i.e., TIM3$^+$VISTA$^+$ TAMs. This TAM niche was specific to nonimmunogenic tumors with low neoantigenic burden and resistance toward PD(L)1 blockade (Fig. 8). This enrichment was mediated by IL-4 signaling. However, just enrichment of these TAMs was not enough to therapeutically target them in vivo. This mandated engagement of these TAMs via ICD induced by chemotherapy (Fig. 8). A "two-signal threshold model for immune inhibition" (*59*) seemed to explain the engagement between ICD and TIM3$^+$VISTA$^+$ TAMs. ICD-driven autocrine type I IFNs provided the "activation signal," while, simultaneously, the HMGB1 and VISTA exposed by dying/stressed cells provided the "inhibitory signal." Consequently, HMGB1/VISTA-based engagement of TIM3/VISTA on TAMs imposed an inhibitory threshold on the ability of these TAMs to mount an ISG response to ICD-derived type I IFNs. This disrupted ICD's ability to activate these TAMs (Fig. 8). However, the blockade of TIM3/VISTA released this inhibition of ISGs and, hence, ICD-inducing PTX synergized with TIM3/VISTA blockade to reduce growth of immunoresistant tumors. Mechanistically, this combination caused repolarization of TIM3$^+$VISTA$^+$ TAMs toward a proinflammatory, ISG response$^+$ phenotype that orchestrated TAM-driven cytotoxicity against cancer cells via TRAIL signaling (Fig. 8). Notably, the failure of TIM3/VISTA blockade alone or with PD1 coblockade in regressing murine tumors, irrespective of their immunogenic profiles, recapitulated a similar failure of these regimen in recent multicancer clinical trials for both TIM3 and VISTA (*9*, *10*).

Our study reverse-translated human characteristics of TIM3$^+$VISTA$^+$ TAMs extracted from large-scale single-cell mapping into representative murine tumors. Thereafter, using mechanistic and translational approaches, we uncovered a multimodal immunotherapeutic strategy to target these TAMs in vivo, thereby blunting immunoresistant tumors. Treatment of low (neo)antigenic and nonimmuno genic tumors is a major unmet clinical need since these tumors do not respond to currently approved ICBs (*23*, *50*, *60*, *61*). Thus, our study has major implications for providing an immunotherapeutic solution not only tailored to overcome immunoresistant tumors but also tailored to blunt their most dominant immunoresistant compartment, i.e., TAMs. In addition, we successfully "translated" the TIM3$^+$VISTA$^+$ TAM signature as pan-cancer biomarker with prognostic and immunotherapy-predictive utility in clinical cohorts.

We also demonstrated that the TIM3$^+$VISTA$^+$ coexpression phenotype is specific to TAMs in both human and mouse and not applicable to other immune cells including various subsets of DCs or T cells. For TIM3, various studies have proposed that almost all of its myeloid protumor activity is driven by TIM3$^+$DCs [especially conventional DC 1(cDC1)], independent of TIM3$^+$TAMs, particularly in the settings of mammary carcinoma or MC38/MC38-OVA tumors (*18*, *19*, *62*). In these studies, DC-specific deletion of TIM3 was essential for tumor control via CD8$^+$ T cell–driven cytotoxicity. We believe that we can exclude a role for this DC–CD8$^+$ T cell axis in our setting due to following observations: (i) Antitumor synergism between PTX and TIM3/VISTA blockade did not activate DC maturation or CD8$^+$ T cell cytotoxicity in vivo; (ii) *HAVCR2*$^+$*VSIR*$^+$ (human/mouse) or *TIM3*$^+$*VISTA*$^+$ (mouse) phenotype was not strongly observed in tumoral DCs and was negligible in cDC1 cells; (iii) a clodronate liposomes dosage that selectively depleted MΦs, but not DCs, completely disrupted synergism of PTX and TIM3/VISTA blockade; (iv) selective and conditional genetic codeletion of TIM3 and VISTA in CSF1R$^+$TAMs was sufficient to render the tumor susceptible to PTX monotherapy in vivo; and (v) CD8$^+$ T cells were dispensable for tumor control. Last, TIM3 was shown to directly suppress type I IFN production from DCs (*18*, *62*). However, in our setting, TIM3/VISTA primarily disrupted the MΦ-intrinsic ISG responses. Although this suggests lack of TIM3/VISTA$^+$DCs involvement in our low antigenic settings, we cannot exclude their role in other contexts with sufficient antigenicity or a proinflammatory milieu (*18*, *62*). Similarly, while association of VISTA with myeloid cells, including TAMs, has been acknowledged, this was still from the perspective of MΦ/DC-driven inhibition of CD8$^+$ T cells (*55*, *63*). Moreover, the mechanism of VISTA-driven

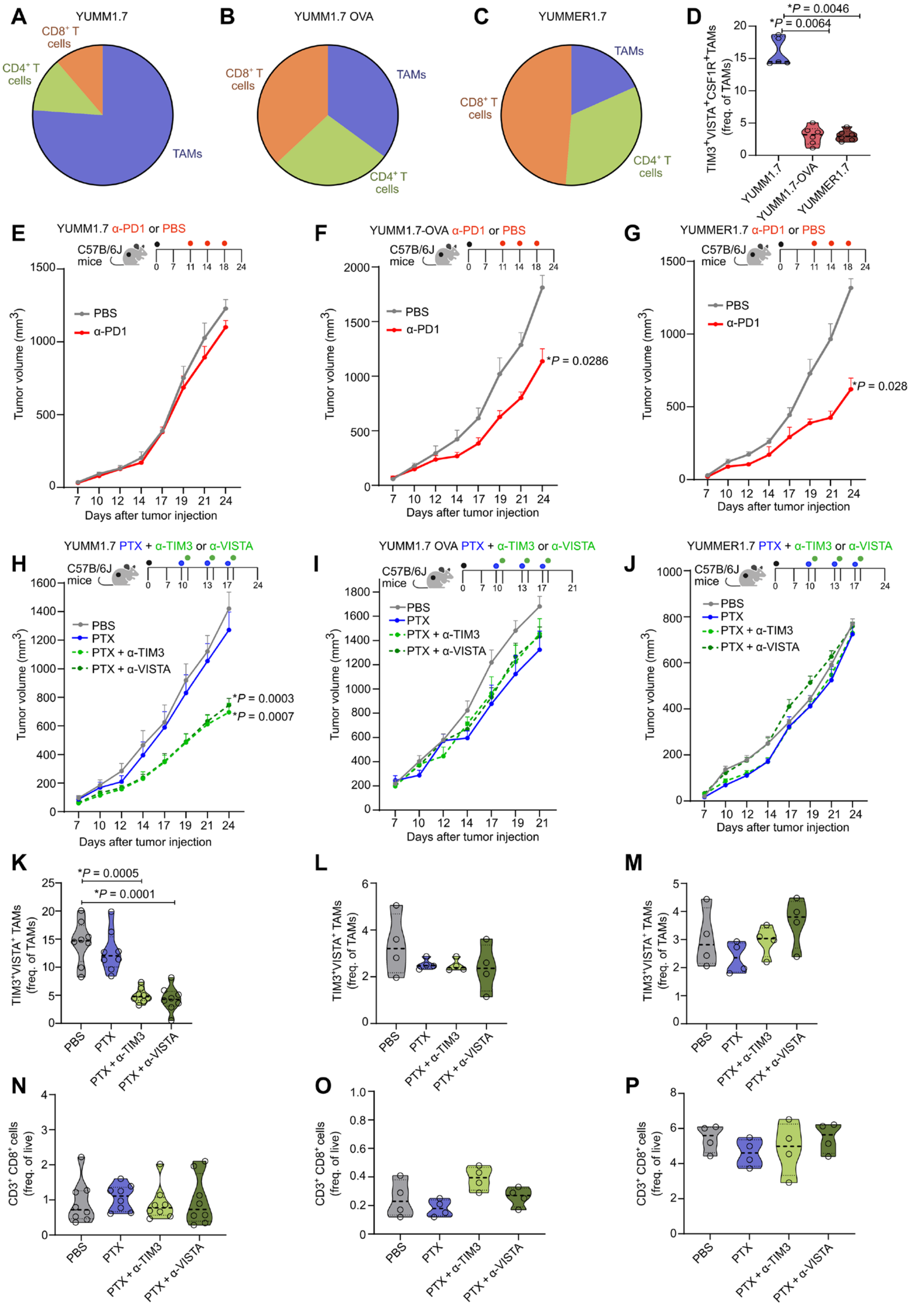

Fig. 7. Targeting TIM3$^+$VISTA$^+$ TAM blunts immunoresistant and low neoantigen melanoma. (**A** to **C**) Basal immunophenotyping of (A) YUMM1.7, (B) YUMM1.7-OVA, and (C) YUMMER1.7 tumors showing percentages of CD8$^+$ T cells, CD4$^+$ T cells, and TAMs (*n* = 6). See fig. S14 (A to C) for the violin plots and statistics corresponding to these pie charts. (**D**) Flow cytometry analysis of CD45$^+$ cell fraction obtained from subcutaneous YUMM1.7, YUMM1.7-OVA, and YUMMER1.7 tumors. Percentage of TIM3$^+$VISTA$^+$CSF1R$^+$TAMs (YUMM1.7, *n* = 5; others, *n* = 6; Mann-Whitney test). (**E** to **G**) Tumor volume curve of (E) YUMM1.7, (F) YUMM1.7-OVA, and (G) YUMMER1.7 tumor–bearing mice treated with anti-PD1 antibody (*n* = 4; Kruskal-Wallis test corrected for FDR). (**H** to **J**) Tumor volume curve of (H) YUMM1.7, (I) YUMM1.7-OVA, and (J) YUMMER1.7 tumor–bearing mice treated with PTX or PBS and/or combination with anti-TIM3 or anti-VISTA antibody (YUMM1.7, *n* = 8; others, *n* = 4; Kruskal-Wallis test corrected for FDR). (**K** to **P**) Flow cytometry analysis of CD45$^+$ cell fraction obtained from subcutaneous YUMM1.7, YUMM1.7-OVA, and YUMMER1.7 tumors treated with PTX or PBS and/or combination with anti-TIM3 or anti-VISTA antibody. (K to M) Percentage of TIM3$^+$VISTA$^+$CSF1R$^+$ TAMs, YUMM1.7 (K), YUMM1.7-OVA (L), and YUMMER1.7 (M) subcutaneous tumors (YUMM1.7, *n* = 8; others, *n* = 4; Kruskal-Wallis test corrected for FDR). (N to P) Percentage of CD3$^+$CD8$^+$ T cells of live cells in YUMM1.7 (N), YUMM1.7-OVA (O), and YUMMER1.7 (P) subcutaneous tumors (YUMM1.7, *n* = 8; others, *n* = 4; Kruskal-Wallis test corrected for FDR). *N* number represents the number of biological repeats or number of independent animals used.

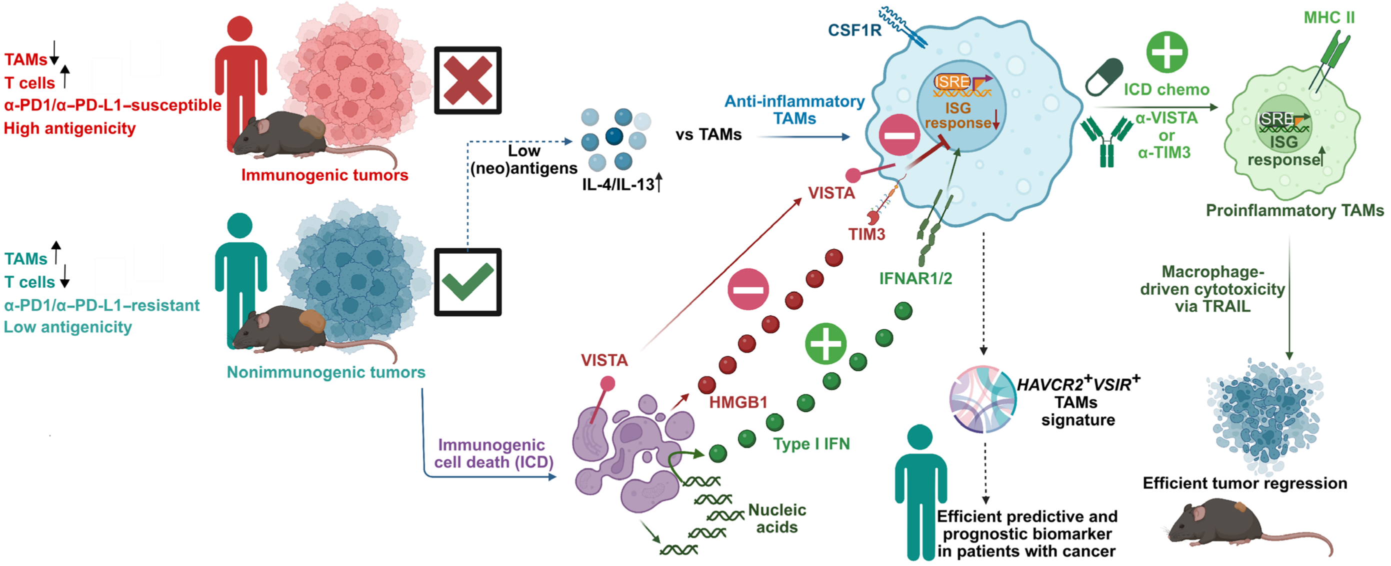

Fig. 8. Study overview. Schematic overview of our study's results and translational as well as clinical value (created with BioRender.com).

TAM suppression has not been sufficiently demonstrated. Our study fills these gaps in current literature.

In conclusion, we show VISTA and TIM3 as redundant suppressors of TAM-associated ISG responses and TAMs-autonomous antitumor cytotoxicity (independent of $CD8^+$ T cells), together with a cross-species map of *HAVCR2*$^+$*VSIR*$^+$TAM features. These are all observations that have not been reported in earlier studies. This offers exciting immunotherapy-tailoring opportunities for TAM-enriched tumors that are insufficiently susceptible to $CD8^+$ T cell–centric approaches.

MATERIALS AND METHODS

Experimental design

The primary objective of this study was to determine the antitumor response and gain mechanistic insights into combination therapy of chemotherapy and immune checkpoint inhibitors in different mouse models consisting of immunogenic and nonimmunogenic tumors. Primary outcomes for in vivo therapy studies included tumor growth measurements and weight loss measurements. In vitro mechanistic studies used enzyme-linked immunosorbent assay (ELISA), IFN/ISG response via J774 reporter MΦs, quantitative polymerase chain reaction (qPCR), Western blot analysis, and flow cytometry analysis. This study used wild-type LLC, MC38, LLC-OVA, YUMM1.7, YUMM1.7-OVA, and YUMMER1.7 tumors in C57BL/6J wild-type or *ifnar1*$^{-/-}$ mice to evaluate and confirm the effects of combination therapy of chemotherapy (PTX and CDDP) and immune checkpoint inhibitors (anti-TIM3 and anti-VISTA). The role of T cells and MΦs was studied by depletion of $CD8^+$ T cells via anti-CD8 antibody and by depletion of MΦs via clodronate liposomes carefully dosed so they only deplete MΦs. Because we specially wanted to see the effect of depletion of our identified MΦ subset, we used hemopoietic stem cells from LSL-Cas9/Csf1r:Cre-ERT mice where CRISPR-Cas9–mediated *Vsir* and *Havcr2* knockout in $CSF1R^+$ cells (MΦs) via in vivo genome editing was done. For all experiments, the number of animals in each group and *P* values are reported in the figure legends. The reported replicates refer to biological replicates. Tumor-bearing mice were randomized into different treatment groups, and weight loss measurements and tumor measurements were monitored blindly.

Experimental models

Mouse models

Wild-type C57BL/6J mice were obtained from the KU Leuven breeding facility. The Ifnar1$^{-/-}$ mice (B6.129S2-Ifnar1tm1Agt/Mmjax) were a gift from the laboratory of R. Vandenbroucke (VIB-Ugent). MΦ-specific TIM3 VISTA knockout mice were generated by intercrossing the tamoxifen-inducible Csf1r:Cre-ERT (a gift of J. W. Pollard from the University of Edinburgh, Scotland) with LoxP-STOP-LoxP Cas9 mice [B6J.129(B6N)- Gt(ROSA)26Sortm1(CAG-Cas9*,-EGFP)Fezh/J], purchased from the Jackson Laboratory. Acute deletion of TIM3 VISTA in MΦs was obtained by daily intraperitoneal injection of tamoxifen (0.05 mg/g of body weight) for 5 days after bone marrow reconstitution. Two days after the tamoxifen cycle, tumor cells were injected. Control mice were treated with tamoxifen according to the same protocol. All subcutaneous tumor experiments were done using 7- to 12-week-old female/male mice, maintained in the conventional mouse facility.

Cell lines

LLC, LLC-OVA, MC38, YUMM1.7, and YUMM1.7-OVA cancer cells were a gift from the laboratory of M. Mazzone (VIB–KU Leuven). Overexpression of OVA in LLC and YUMM1.7 cancer cells were generated as previously described (*64*). YUMMER1.7D4 cancer cells were bought from Merck Millipore. J774-DUAL cells, a murine MΦ-like cell containing a nuclear factor κB (NF-κB)–secreted embryonic alkaline phosphatase (SEAP) and IFN regulatory factor (IRF)–lucia reporter, were bought from InvivoGen. CRISPR-Cas9 knockout LLC cancer cells for CEACAM1, HMGB1, Galectin-9, PSGL1, and VISTA were generated by the laboratory of D. Daelemans (Rega Institute–KU Leuven).

All cell lines were cultured at 37°C under 5% CO_2 split when 90% confluency was reached through enzymatic dissociation

(Trypsin). MC38, LLC, and LLC-OVA cells were maintained in Dulbecco's modified Eagle's medium (DMEM) containing 2 mM L-glutamine, sodium bicarbonate (3.7 g/liter), glucose (4.5 g/liter), and 1.0 mM sodium pyruvate with 10% heat-inactivated fetal bovine serum (FBS; 30 min at 56°C), penicillin (100 U/ml), and streptomycin (100 μg/ml). YUMM1.7, YUMM1.7-OVA, and YUMMER1.7D4 were maintained in F12 DMEM containing 2 mM L-glutamine, sodium bicarbonate (3.7 g/liter), glucose (4.5 g/liter), and 1.0 mM sodium pyruvate with 10% heat-inactivated FBS (30 min at 56°C), penicillin (100 U/ml), and streptomycin (100 μg/ml). J774-DUAL cells were maintained according to the manufacturer's protocol. All cell lines were tested for *Mycoplasma* every month.

CRISPR-Cas9–mediated gene knockout in the LLC cell line

Knockouts of *Ceacam1*, *Hmgb1*, *Lgals9*, *Selplg*, and *Vsir* genes were generated using four different guides per gene [single gRNA (sgRNA) target sequences are in the Supplementary Materials]. Guide sequences were cloned into the pLentiCRISPRv2 plasmid according to the standard cloning protocol. For lentiviral particle production, human embryonic kidney (HEK) 293T cells (received from J. Moffat, Donnelly Centre, University of Toronto, Canada) were plated in 40-ml supplemented DMEM in T150 (TPP) flasks at 45% confluency and incubated overnight. Twenty-four hours later, the cells were cotransfected using X-TremeGENE 9 with the pLentiCRISPR plasmids and the lentiviral packaging plasmids pMD2.G and psPAX2 to generate lentiviral particles coated with the vesicular stomatitis virus glycoprotein protein and incubated overnight. Twenty-four hours after transfection, the medium was changed to DMEM supplemented with serum-free bovine serum albumin (BSA) growth medium [DMEM + BSA (1.1 g/100 ml) and gentamicin (20 μg/ml)]. The supernatant containing lentiviral particles was harvested 72 hours after transfection and stored at −80°C. Cells were transduced with lentiviruses expressing a pool of the four sgRNAs and then selected with puromycin for 3 days. Knockout phenotype was confirmed by Western blotting.

Method details

Cell death induction

For cell death induction, cells were seeded in the appropriate dish as such that they reached an 80% confluency the next day. Apoptosis was induced by adding 100 μM CDDP (Sigma-Aldrich, #p4394) or 100 μM PTX (Sigma-Aldrich, #T1912). In case of coincubation experiments, cells were scraped and collected after 24 hours of cell death induction, washed in PBS, counted, and cocultured.

Thiazolyl blue tetrazolium bromide assay

LLC and MC38 cells were seeded in a 96-well plate at a density of 5000 cells per well 24 hours before cell death induction. Cell survival was obtained using the thiazolyl blue tetrazolium bromide (MTT) reagent (Abcam, #ab197010). Absorbance was read on a microplate reader (BioTek) at 490 nm at 24 and 48 hours after cell death induction. For all values, fold change to UT cancer cells was taken and multiplied with 100 to obtain a percentage.

J774 MΦ reporter assay

J774-DUAL reporter cells were seeded in a 96-well plate at a density of 30,000 cells per well in a 96-well plate. After 24 hours, cells were pretreated with isotype (10 μg/ml) or blocking antibodies for 4 hours. UT and treated cancer cells were cocultured with the J774-DUAL reporter cells in a 1:1 ratio. In the case of neutralizing nucleic acids, UT and treated cancer cells were preincubated for 1 hour before with 3350 U/10^6 cancer cell DNase I (Invitrogen, #18047-019) and 3.350 mg/10^6 cancer cell RNase A (Thermo Fisher Scientific, #EN0531). Thereafter, cancer cells were cocultured with the J774-DUAL reporter cells in a 1:1 ratio. To measure the IFN (IRF)/ISG response after 48 hours, another 80 μl of medium was derived from the above cancer cell–J774 coculture in a white opaque-bottom 96-well plate. Here, 50 μl of Quanti-LUC substrate (Invivogen, #rep-qlc2) was added, and bioluminescence was directly measured with 100 ms of signal integration, with the microplate reader. All data derived from this reporter assay were minimum-maximum normalized for percentage scaling to account for interassay baseline variability.

Western blot

For intracellular proteins, 800,000 cells were seeded in 10-cm dishes 24 hours before cell death induction. Cells were scraped and collected at 6, 24, or 48 hours after cell death induction. Cells were centrifuged at 1500 rpm for 5 min, and the pellet was resuspended in 100 μl of NP-40 lysis buffer (Thermo Fisher Scientific, #FNN0021) with protease (Thermo Fisher Scientific, #A32953) and phosphatase inhibitors (Thermo Fisher Scientific, #A32957). For secreted proteins, cells were 2,500,000 cells seeded in 15-cm dishes, and medium was collected 24 hours after cell death induction. Floating cells were removed by centrifugation. The supernatant was concentrated using Amicon Ultra-15 centrifuge filter units (Merck, #UFC901024). A bicinchoninic acid assay (BCA) for colorimetric quantification of total protein was done with a BCA protein assay kit (Thermo Fisher Scientific, #23227) and a protein mixture of 90 μg was loaded onto the gel. The following proteins were detected: caspase 9 and cleaved caspase 9 (clone C9), VISTA (D5L5T), PSGL-1 (clone HECA-452), Ceacam-1 (clone E-12), Galectin-9 (clone D9R4A), HMGB1 (clone EPR3507), and β-actin (clones AC-74 and AC-15). The primary antibodies were diluted in 5% BSA + Tris-buffered saline with 0.1% Tween 20 detergent (TBST) with a dilution factor of 1:1000. As secondary antibody, we used the anti-rabbit antibody labeled with horseradish peroxidase (HRP) (Cell Signaling Technology, #7074S), anti-mouse antibody labeled with HRP (Cell Signaling Technology, #7076S), or anti-rat antibody labeled with HRP (Cell Signaling Technology, #7077S) diluted in 5% BSA + TBST with a dilution factor of 1:2000. The antibodies tethering to the proteins on the membranes were detected using the enhanced chemiluminescence substrate, and the resulting precipitate was detected with the ChemiDoc MP imaging system. The precision plus protein dual color standards (Bio-Rad, #161037) was used as a ladder.

ATP secretion

Medium of LLC and MC38 cells after cell death induction was harvested at 6, 24, and 48 hours. The presence of ATP in the medium was analyzed using the ATP assay system (Promega, #FF2000). A fold change to UT cells was taken to obtain ATP release.

Enzyme-linked immunosorbent assay

BMDM cocultures with LLC (UT and treated) cancer cells were made as described above and used to perform an IFN-β ELISA (Invivogen #luex-mifnbv2). The IFN-β ELISA was performed according to the manufacturer's protocol.

Subcutaneous wild-type LLC/MC38 or LLC-OVA tumors were treated with PTX or PBS in combination with anti–TIM3 antibody (α-TIM3) or anti–VISTA antibody (α-VISTA) as described in the "Mouse experiments" section. Tumors were taken on day 24 after tumor cell injection, and whole-tumor lysate was made IL-4 ELISA (BioLegend, #431101) and IL-13 ELISA (Thermo Fisher Scientific,

#431101) was done with whole-tumor lysate according to the manufacturer's protocol. Absolute values were used to take a ratio with the blank. Thereafter, a ratio of IL-4/IL-13 to total TAMs was taken.

Flow cytometry–based detection of calreticulin, CD47, and HSP90

A total of 200,000 LLC and MC38 cells were plated in 12-well plates in 1 ml of DMEM and incubated for 24 hours. Cell death was induced for 48 hours. Then, the cells were collected, washed with PBS, and transferred to 5 ml of flow cytometry tubes. The cells were resuspended in 50 μl of fluorescence-activated cell sorting (FACS) buffer (0.5% BSA and PBS solution) and 1:100 anti-calreticulin primary antibody (clone B44) or 1:100 anti-HSP90 primary antibody (clone AC88). After 30-min incubation in the dark on ice, cells were washed with 1 ml of FACS buffer and centrifuged, and the supernatant was discarded. Then, cells were again resuspended in 50 μl of FACS buffer with 1:500 of goat anti-rabbit Alexa Fluor 488 (polyclonal) for calreticulin or 1:500 goat anti-Mouse secondary antibody for HSP90 (polyclonal), anti-CD47 (clone miap301) antibody, and Fixable Viability Dye eFluor 780. After 30-min incubation on ice in the dark, cells were fixed with Cytofix (BD Biosciences, #554655).

Flow cytometry

Before staining procedure, Fc receptors of all samples were blocked using TruStain FcX (BioLegend, #101320) for 15 min. Cells were further stained with the indicated antibodies listed in table S2, diluted in 0.5% BSA for 1 hour, and fixed with Cytofix (BD Biosciences, #554655). In case of intracellular markers, cells were fixed and permeabilized with the Cytofix/Cytoperm Kit (BD Biosciences, #554714). For the staining of transcription factors, the true nuclear transcription factor buffer (BioLegend, #42441) set was used. After fixation, cells were maintained in 0.5% BSA. For intracellular cytokine staining, the cells were stimulated with Dynabeads Mouse T activator CD3/CD28 (Thermo Fisher Scientific, #11456D). After 1 hour at 37°C and 5% CO_2, 2 μl of brefeldin A (Thermo Fisher Scientific, #00-4506-51) was added. Cells were then placed at 37°C and 5% CO_2 for 4 hours, transferred to 4°C overnight, and then stained for intracellular cytokines. Flow cytometry was performed on the Attune NxT (Thermo Fisher Scientific), FACSCanto (BD Biosciences), or the ID7000 (SONY). Cell doublets were excluded on the basis of forward scatter area (FSC-A)/forward scatter height (FSC-H). Flow cytometry data were analyzed using FlowJo. Gating strategies and unstained and fluorescent minus one controls are shown in the Supplementary Materials.

Murine splenocyte isolation

Splenocytes were obtained from the spleen from wild-type C57BL/6J mice. Spleens were minced and filtered through a 70-μm cell strainer. Cells were incubated in red blood cell lysis buffer for 5 min and centrifuged.

Murine tumor-infiltrating leukocytes and TAM isolation

Tumors were isolated at day 24 after tumor injection. A single-cell suspension was made, using the tumor dissociation kit (Miltenyi, #130-096-730). Tumor-infiltrating leukocytes (TILs) were isolated through magnetic bead separation via CD45 (Miltenyi, #130-110-618). For TAM isolation, anti-F4/80 microbeads (Miltenyi, #130-110-443) were used. Isolated TILs and TAMs were maintained in RPMI 1640 supplemented with penicillin (100 μg/ml), streptomycin (100 μg/liter), 2.5% Hepes (pH 7.5), and 10% heat-inactivated FBS. The following fluorochrome-conjugated antibody clones were used: FOXP3 (clone MF-14), GATA3 (clone TWAJ), CD62L (clone MEL-14), TCF1/7 (clone S33-966), CD107a (clone 1D4B), TOX (clone REA473), Tbet (clone O4-46), CD3 (clone 17A2), CD8a (clone 53-6.7), Ki67 (clone 11F6), CD45 (clone 30-F11), Eomes (clone Dan-11mag), CD127 (clone SB/199), PD1 (clone RMP1-30), CD4 (clone GK1.5), TIM3 (clone 5D12/TIM-3), IL-2 (clone JES6-5H4), TNFα (clone MP6-XT22), IFN-γ (clone XMG1.2), PDL1 (clone 10F.9G2), PD1 (clone 29F.1A12), Siglec H (clone 551), CD11c (clone N418), XCR1 (clone ZET), CD172A (clone P84), MHCII (clone M5/114.15.2), PD-L1 (clone 10F.9G2), PD1 (clone RMP1-30), CD86 (clone GL1), F4/80 (clone T45-2342), CSF1R (clone AFS98), CD11b (clone ICRF44), TIM3 (clone B8.2C12), VISTA (clone MH5A), and CD206 (clone C068C2).

Cancer cell–TAM cocultures

LLC cancer cells were cocultured with LLC tumor–derived TAMs (preincubated with isotype blocking antibodies or anti-TIM3/anti-VISTA blocking antibodies) in a 1:5 ratio. After 24, 48, and 72 hours, cocultures were scraped to collect the cells, centrifuged, and washed with PBS. Single-cell suspension was stained with fluorescently labeled antibodies diluted in FACS buffer (0.5% BSA and PBS solution) for 1 hour on ice and then washed twice with staining buffer (BioLegend, #420201). Thereafter, cells were washed once in 1× annexin V binding buffer (BioLegend, #422201) and stained with fluorescently labeled annexin V antibody diluted in 1× annexin V binding buffer. After 15 min of staining at RT, samples were washed once, then resuspended with 1× annexin V binding buffer, and analyzed immediately at the flow cytometer. The following fluorochrome-conjugated antibody clones were used before annexin V staining: F4/80 (clone T45-2342), CD11b (clone ICRF44), Fixable Viability Dye eFluor 780, and annexin V.

Quantitative polymerase chain reaction

The RNA of cancer cell–TAM cocultures was extracted using the PureLink RNA Mini Kit (Thermo Fisher Scientific, #12183025). Using the QuantiTect Reverse Transcription kit (QIAGEN, #205313), cDNA was synthesized from RNA. The qPCR was performed on the StepOnePlus Real-Time PCR system (Applied Biosystems) using SYBRgreen (HighQu, #QPD0150) with the following primers: *Irf7*, *Rsad2*, *Mx1*, *Cxcl10*, and *Actin* (all primers were ordered at Integrated DNA Technologies, sequences available inthe Supplementary Materials). Fold change was determined using the $2^{\Delta\Delta CT}$ method compared to the house keeping gene, *Actin*, and UT TAMs.

Antibody array

At day 24, tumors were collected from PBS, PTX, PTX + TIM3, and PTX + VISTA mice. $CD45^+$ fractions were used to prepare tumor lysate with NP-40 lysis buffer, and protein concentration was measured. A protein concentration of 200 μg was used for a mouse cytokine array panel A (R&D Systems, #ARY006). Cytokine array was performed according to the manufacturer's protocol. Arrays were read on the ChemiDoc (Bio-Rad). Dot intensities were determined using Image Lab (Bio-Rad). From all values, the background was subtracted.

Efferocytosis assay

A total of 30,000 BMDMs were plated in white clear–bottom 96-well plate (Corning, #3610) per well. BMDMs were either pretreated with 20 μM cytochalasin D for 3 hours as a negative control or pretreated with isotype (10 μg/ml) or blocking antibodies for 4 hours. UT or dying cancer cells were collected 24 hours after cell death induction. Cells were stained with pHrodo Green (20 μg/ml; Thermo Fisher Scientific, #P35373) for 1 hour and washed with FBS. Cells were added to BMDMs in a 1:1 ratio. Plates were kept in 37°C under 5%

CO_2. Fluorescence at an excitation of 490 nm and an emission of 520 nm were measured at 24 and 48 hours after coincubation on a microplate reader (BioTek). Efferocytosis index was calculated with the following formula: (fluorescence intensity 37°C − fluorescence intensity cytochalasin D) × (fluorescence intensity cancer cells 37°C / MTT percentage). MTT assay was performed as described above. In the case of efferocytosis with pHrodo Green *E. coli* BioParticles (Thermo Fisher Scientific, #P35366), a concentration of 200 ug/ml was used.

TIM3$^+$VISTA$^+$ TAM and TIM3$^-$VISTA$^-$ TAM cocultures with PTX

Murine TILs were collected from LLC tumor–bearing mice as described above. Single-cell suspension was stained with F4/80 (clone T45-2342), Fixable Viability Aqua Zombi, TIM3 (clone B8.2C12), and VISTA (clone MH5A). Samples were sorted on the BD influx cell sorter to obtain TIM3$^+$VISTA$^+$ TAMs and TIM3$^-$VISTA$^-$ TAMs (see gating strategy). From each sample, 100,000 TIM3$^+$VISTA$^+$ TAMs and TIM3$^-$VISTA$^-$ TAMs were plated in a duplicate 12-well plate. The next day, 20,000 LLC cancer cells were added to all the TAMs and also plated alone. After 48 h of coculture, half of the samples were treated with 100 μM PTX, and the rest was left UT. Cocultures were scraped to collect after 48 hours of treatment, centrifuged, and washed with PBS. Single-cell suspension was stained with fluorescently labeled antibodies diluted in FACS buffer and analyzed immediately at the flow cytometer. The following fluorochrome-conjugated antibody clones were used: CD11b (clone ICRF44), Fixable Viability Aqua Zombi, and Ki67 (clone 11F6).

TAM cytotoxicity assay

Murine TAMs were collected from LLC tumor–bearing mice treated with PBS or PTX as described above. A total of 30,000 TAMs were plated in a 96-well plate per well. After 24 hours, TAMs were preincubated with either one of the following inhibitors for 4 hours: 100 μM apocynin, catalase (1000 U/ml), 100 μM L-NMMA, 10 μM anti-TNFα, 10 μM anti-FasL, or 10 μM of anti-TRAIL. After 4 hours, 30,000 UT LLC cancer cells were added to the TAMs with either anti-TIM3 (10 μg/ml) or anti-VISTA (10 μg/ml) or no blocking antibody. After 48 hours of coculture, all the samples were stained with fluorescently labeled antibodies diluted in FACS buffer and analyzed immediately at the flow cytometer. The following fluorochrome-conjugated antibody clones were used: CD11b (clone ICRF44), Fixable Viability Aqua Zombi, and Ki67 (clone 11F6).

Murine BMDM generation

Bone marrow was isolated from wild-type C57BL/6J or Ifnar1$^{-/-}$ mice. Both the femur and tibia were flushed using PBS, and the cell suspension was centrifuged for 5 min at 1500 rpm. The pellet was resuspended in red blood cell lysis buffer (Merck Life Science), incubated for 5 min, and centrifuged. Cells were resuspended in RPMI 1640 supplemented with penicillin (100 U/ml), streptomycin (100 μg/liter), 2.5% Hepes (pH 7.5), and 10% heat-inactivated FBS. Bone marrow–derived cells were differentiated into MΦs by adding macrophage colony-stimulating factor (25 ng/ml; Peprotech, #315-02) into the medium for 6 days. Differentiation of MΦs was confirmed by flow cytometry; the following fluorochrome-conjugated antibody clones were used: CD11b (clone M1/70) and F4/80 (clone BM8).

In vitro and in vivo targeting of Havcr2 and Vsir

To validate the knockout of TIM3 and VISTA, lentiCRISPRv2 vectors expressing the Cas9 along with a dual gRNA targeting *Havcr2* (TIM3) locus (GTTACACTCTATCTACACCT) and *Vsir* (VISTA) (GGGTGATAGAGAAGTTACCG) or a nontargeting control gRNA (GAACAGTCGCGTTTGCGACT) were used. The lentiCRISPRv2 was a gift from F. Zhang (Addgene, plasmid no. 52961) (*65*). The gRNAs were cloned as previously described by Shang *et al.* (*66*). Lineage-negative HSPCs from LSL-Cas9/CSF1R-creERT transgenic mice were enriched with the mouse hematopoietic progenitor enrichment kit (STEMCELL Technologies). A total of 1 × 10^6 cells/ml were prestimulated for 5 hours with stem span serum-free medium (STEMCELL Technologies) supplemented with IL-3 (20 ng/ml), stem cell factor (SCF) (100 ng/ml), thrombopoietin (TPO) (100 ng/ml), and FMS-like tyrosine kinase 3 ligand (FLT-3L) (100 ng/ml) (Peprotech) and transduced with purified lentiviral vectors in the presence of polybrene for 48 hours. After adding virus, cells were centrifuged for 1 hour at 1000*g* at RT. Cells were monitored over time, and a second spin infection was performed. Seven hours later, 1 × 10^6 cells were injected via tail vein in lethally irradiated C57BL/6-recipient mice. A fraction of transduced HSPCs were either collected for FACS analysis or differentiated into BMDMs.

Cell culture and transfection

HEK293T were cultured in DMEM (Gibco) supplemented with 10% heat-inactivated FBS (Gibco), 2 mM L-glutamine (Life Technologies), and penicillin (100 U/ml)/streptomycin (100 μg/ml) (Life Technologies). Cells were maintained in a humidified incubator at 37°C and 5% CO_2. To generate lentiviral particles, HEK293T cells were seeded at 9 × 10^6 cells in 20 ml in 15-cm dishes and transfected the following day. Two hours before transfection, medium was changed to Iscove's modified Dulbecco's medium supplemented with 10% FBS (Gibco), 2 mM L-glutamine (Life Technologies), and penicillin (100 U/ml)/streptomycin (100 μg/ml) (Life Technologies).

Transfection was done by the calcium phosphate method with 32 μg of transfer vector carrying the respective sgRNAs for TIM3 and VISTA or the nontargeting gRNA as control. Each transfection also included 7 μg of a plasmid encoding PMD2.G and 16.25 μg of a plasmid encoding packaging proteins. Virus was collected 24 and 48 hours after transfection, filtered, and concentrated via ultracentrifugation.

In vivo experiments

Mouse experiments

Seven- to 12-week-old female/male C57BL/6J mice or Ifnar1$^{-/-}$ mice were subcutaneously injected with 1 × 10^6 LLC, LLC-OVA, MC38, YUMM1.7, YUMM1.7-OVA, YUMMER1.7, LLC HMGB1$^{-/-}$, or LLC VISTA$^{-/-}$ cells. In the case of chemotherapy, mice were treated with CDDP (8 mg/kg) or PTX (8 mg/kg) on days 10, 13, and 17 via intraperitoneal injections. When applicable, mice were treated or cotreated with 250 μg of anti-PDL1, anti-CTLA4, anti-CSF1R, anti-PD1, anti-TIM3, anti-VISTA, anti-CCL2, anti-SIRPα, anti-CR1/2, anti-TGFβ, anti-FCγRII/III, anti–IL-10, CD40 agonism, or anti–IL-1β on days 11, 14, and 18 via intraperitoneal injections. For CD8 depletion experiments, mice were given 200 μg of anti-CD8, intraperitoneally 1 day before tumor inoculation and, from then on, every other day. For IL-4 depletion experiments, mice were given 500 μg of anti–IL-4, intraperitoneally 2 days before tumor inoculation and, from then on, every other day. For MΦ depletion experiments, 200 μl of clodronate liposomes was given 1 day before tumor inoculation and every 2/3 days subsequently. Mice were monitored and weighed every other day, and tumor volume was determined by height ×

width × length. Please see table S2 for further reference to the used clones.

Bone marrow transplantation

To generate TIM3 VISTA bone marrow chimera, 7- to 8-week-old C57BL/6J-recipient mice were lethally irradiated with 9.2 Gy using the Small Animal Radiation Research Platform (XSTRAHL). Subsequently, 1×10^6 bone marrow cells from the appropriate genotype were injected intravenously via the tail vein. Tumor experiments were initiated 6 weeks after bone marrow reconstitution. Red and white blood cell count was determined using a hematocytometer on peripheral blood, collected in heparin with capillary pipettes by retro-orbital bleeding.

Bioinformatics analyses

Transcriptomics analyses for murine subcutaneous tumors

Affymetrix Mouse Exon 1.0 ST Array data associated with GSE85509 was downloaded from the Gene Expression Omnibus (*67*). This study includes a range of subcutaneous tumors based on B16-F10, TC1, CT26, MC38, LL2/LLC, RENCA, 4 T1, TRAMPC1, EL4, P815, or PAN02 murine cancer cell lines implanted in syngeneic mice backgrounds (*37*). Genetic signatures of proimmunogenic IFN-γ signaling versus MΦs were used to classify these tumors (*20*, *21*, *23*–*27*, *35*, *37*). For the differential analysis between LLC and MC38, corresponding CEL files were downloaded and normalized with the Robust Microarray Analysis (RMA) method, using oligo 1.60.0 (*68*) in R 4.2.0 (*69*). Probe expression was subsequently summarized to the gene level using the associated Affymetrix NetAffx CSV file (MoEx-1_0-st-v1.na28.mm9.transcript.csv). Statistical significance of differences between LLC and MC38 was assessed with limma 3.52.2 (*70*), using t tests with empirical Bayesian shrinkage of the variance. P values were corrected for multiple testing following the Benjamini-Hochberg method. Results were represented as volcano plots. A select set of immune-relevant genes was highlighted with text labels.

Transcriptomic analysis in TCGA

Bulk transcriptomics count data from the TCGA Toil-recompute project (*71*) were downloaded from UCSC Xena (*72*). Survival information was obtained from the same data hub. Immune classifications, delineating distinct immune subtypes in TCGA (C1 to C6; see Results for more details), were obtained from the supplementary files associated with the "The immune landscape of cancer" study (*73*) (table S1), which lists calls for 11,081 samples. Precalculated immune deconvolutions for TCGA were downloaded from TIMER 2.0 (*74*), which contains a total of 11,071 samples. In this study, we only used the quanTIseq (*75*) calls. The dataset was subset to only include primary tumors, recurrent tumors, metastatic tumors, and "additional new primary" or "additional metastatic" samples, resulting in a data matrix containing 9611 samples with RNA-seq, of which 8549 contained survival information and MΦ quantification.

Spearman correlations between a TIM3-VISTA metagene and the corresponding quanTIseq-deconvoluted MΦ population were calculated per immune subtype (C1 to C6) with SciPy 1.6.2 (*76*) and visualized as radar plot, using Matplotlib 3.5.2 (*77*). Samples for which no immune subtype or deconvoluted fraction was available were ignored.

Survival analysis in TCGA

The TCGA dataset described above was used for a prognostic analysis, in which the effect of the expression of the TIM3-VISTA metagene (mean expression of all genes in signature) was associated with the OS, using a Cox regression as implemented in lifelines 0.26.3 (*78*) with default settings. Overall, our analysis included 8516 patients with survival and metagene expression spanning 30 cancer types [Adenoid Cystic Carcinoma (ACC), 76; Bladder Urothelial Carcinoma (BLCA), 395; Breast Invasive Carcinoma (BRCA), 1085; Cervical Squamous Cell Carcinoma and Endocervical Adenocarcinoma (CESC), 301; Cholangiocarcinoma (CHOL), 35; Colon Adenocarcinoma (COAD), 280; Esophageal Carcinoma (ESCA), 171; Glioblastoma Multiforme (GBM), 157; Head and Neck Squamous Cell Carcinoma (HNSC), 513; Kidney Chromophobe (KICH), 65; Kidney Renal Clear Cell Carcinoma (KIRC), 513; Kidney Renal Papillary Cell Carcinoma (KIRP), 277; Liver Hepatocellular Carcinoma (LIHC), 361; Low Grade Glioma (LGG), 519; Lung Adenocarcinoma (LUAD), 446; Lung Squamous Cell Carcinoma (LUSC), 447; Mesothelioma (MESO), 82; Ovarian Cancer (OV), 272; Pancreatic Adenocarcinoma (PAAD), 152; Pheochromocytoma and Paraganglioma (PCPG), 180; Prostate Adenocarcinoma (PRAD), 403; Rectum Adenocarcinoma (READ), 87; Sarcoma (SARC), 226; Skin Cutaneous Melanoma (SKCM), 104; Stomach Adenocarcinoma (STAD), 383; Testicular Germ Cell Tumors (TGCT), 136; Thyroid Carcinoma (THCA), 507; Uterine Corpus Endometrial Carcinoma (UCEC), 177; Uterine Carcinosarcoma (UCS), 57; Uveal Melanoma (UVM), 79]. We noticed an imbalance in SKCM toward the primary tumor samples (104 of 469 SKCM used) as primarily metastatic samples did not have a definite immune subtype assigned by Thorsson and co-workers (*73*). However, this only affected a small proportion of the total pan cancer dataset. HRs were represented as a forest plot, using Matplotlib 3.5.2.

Analysis of scRNA-seq datasets

Single-cell datasets covering patients with melanoma responding (or not) to immunotherapy (PD1/CTLA4 blockade) (*24*), pan-immune dataset from four different cancers (*25*), pan-myeloid dataset from eight different cancers (*26*), and CRC dataset with patients with MSI and MSS CRC (*27*) were accessed using a standardized and uniformized workflow of BBrowser_v_3 (*35*), using built-in qualitative filters. The preexisting scRNA-seq dataset of subcutaneous LLC tumors (*38*) was uploaded into the same workflow and further analyzed to maintain uniformity. This workflow was used for generating density plots or dot plots, as applicable. Cellular annotations either preexisted on the level of author-derived annotations or were based on automated annotations available within the above workflow. We used the *HAVCR2*$^+$*VSIR*$^+$TAMs within the CRC scRNA-seq dataset to perform DGE analyses and codependent pathway enrichment analyses (REACTOME for human and Gene Ontology Biological Process for mouse), using the Venice nonparametric analyses approach (https://github.com/bioturing/signac). This was specifically done by comparing scRNA-seq profiles of *HAVCR2*$^+$*VSIR*$^+$TAMs (*HAVCR2* and *VSIR* expression > 0) versus *HAVCR2*$^-$*VSIR*$^-$TAMs (*HAVCR2* and *VSIR* expression = 0) against each other. Notably, in some datasets, an alternative name for *VSIR* was *C10orf54*. The DGE analyses also allowed us to extract a signature for *HAVCR2*$^+$*VSIR*$^+$TAMs, which included all positively enriched genes in favor of this subset above the statistical cutoff of $-\log_{10}(P \text{ value}) = 100$. With this cutoff, we delineated the following signature for *HAVCR2*$^+$*VSIR*$^+$TAMs (some major TAM genes are indicated in bold): ***C10orf54***, *TYROBP*, ***HAVCR2***, *B2M*, *GRN*, *LAPTM5*, *CD74*, *HLA-C*, *PSAP*, *NPC2*, *TMEM176B*, *VAMP8*, *HLA-A*, *HLA-DMB*, *HLA-DPA1*, *GPX1*, ***CD68***, *HLA-DMA*, *TMSB4X*, *OAZ1*, *HLA-E*, *CFL1*, *ARPC1B*, ***FCGRT***, *ITM2B*, ***C1QC***, *PFN1*,

HLA-B, *HLA-DPB1*, *HLA-DRA*, *CST3*, *ARHGDIB*, *CYBA*, *TMSB10*, *CTSB*, *HLA-DQB1*, *ITGB2*, *ACTG1*, *CAPG*, *ARPC3*, *S100A11*, *RPL15*, *CTSS*, ***C1QB***, *ATP6V0B*, *CTSA*, *RPS2*, *YBX1*, *CTSC*, *PTMA*, *SRP14*, *AIF1*, ***C1QA***, *PPT1*, *CTSH*, *CALM2*, ***CSF1R***, *YWHAH*, *RPL28*, *CAPZB*, *ACTB*, *TYMP*, *CLIC1*, *ATP6V0E1*, *CTSD*, *RPL13A*, *HEXB*, *SERF2*, *EEF1A1*, ***FCER1G***, *ACP5*, *TMEM176A*, *RPS19*, *PLD3*, *CORO1B*, *RPSA*, *RPL27A*, *PYCARD*, *SYNGR2*, *RPS3*, *BST2*, *NACA*, *PRDX1*, *LAIR1*, *PPIA*, and *ERP29*. The full scRNA-seq profile of $HAVCR2^{+}VSIR^{+}$TAMs (*HAVCR2* and *VSIR* expression > 0) was used to drive the automated Cell Ontology analyses (i.e., Cell Search algorithm) to interrogate the 300 scRNA-seq datasets within the curated BioTuring database as available on 17 February 2021 (*35*). The hits were filtered at a Jaccard's index threshold of 0.7. This analyses delineated the following dataset hits for MΦ node: basal cell carcinoma (GSE123814), CRC (GSE144735), liver cancer (GSE125449), lung (COVID-19; GSE145926), lung cancer (E-MTAB-6149), lung cancer (GSE140819), pancreatic cancer [Genome Sequence Archive (GSA) GSA: CRA001160], and testis (normal; GSE134144); and the following datasets are for monocyte node: fetal liver (E-MTAB-7407), lung (PRJEB31843), lung fibrosis (GSE128033), lung fibrosis (GSE121611), lung fibrosis (GSE135893), lung cancer (GSE131907), Scleroderma-associated interstitial lung disease (SSc-ILD) (GSE128169), melanoma (GSE123139), nasopharyngeal cancer (GSE150430), peripheral blood mononuclear cells (sepsis; SCP548), peripheral blood mononuclear cells (SC2018), respiratory tract (EGAS00001004082), and spleen (PRJEB31843).

Immuno-oncology clinical trials analyses

Patient survival analyses in immuno-oncology clinical trials was carried out using the above $HAVCR2^{+}VSIR^{+}$TAMs signature, i.e., *C10orf54*, *TYROBP*, *HAVCR2*, *B2M*, *GRN*, *LAPTM5*, *CD74*, *HLA-C*, *PSAP*, *NPC2*, *TMEM176B*, *VAMP8*, *HLA-A*, *HLA-DMB*, *HLA-DPA1*, *GPX1*, *CD68*, *HLA-DMA*, *TMSB4X*, *OAZ1*, *HLA-E*, *CFL1*, *ARPC1B*, *FCGRT*, *ITM2B*, *C1QC*, *PFN1*, *HLA-B*, *HLA-DPB1*, *HLA-DRA*, *CST3*, *ARHGDIB*, *CYBA*, *TMSB10*, *CTSB*, *HLA-DQB1*, *ITGB2*, *ACTG1*, *CAPG*, *ARPC3*, *S100A11*, *RPL15*, *CTSS*, *C1QB*, *ATP6V0B*, *CTSA*, *RPS2*, *YBX1*, *CTSC*, *PTMA*, *SRP14*, *AIF1*, *C1QA*, *PPT1*, *CTSH*, *CALM2*, *CSF1R*, *YWHAH*, *RPL28*, *CAPZB*, *ACTB*, *TYMP*, *CLIC1*, *ATP6V0E1*, *CTSD*, *RPL13A*, *HEXB*, *SERF2*, *EEF1A1*, *FCER1G*, *ACP5*, *TMEM176A*, *RPS19*, *PLD3*, *CORO1B*, *RPSA*, *RPL27A*, *PYCARD*, *SYNGR2*, *RPS3*, *BST2*, *NACA*, *PRDX1*, *LAIR1*, *PPIA*, and *ERP29*. We accessed tumor transcriptomic data from patients with cancer with pre-/on-treatment samples profiled relative to anti-PD1, anti–PD-L1, or anti-CTLA4 immunotherapy using an existing computational workflow [KMPlot (*79*, *80*)] along with OS or PFS values for these patients (follow-up threshold = 36 months and survival time = days). These data originated from the following cohorts for OS: GIDE2019, GSE121810, GSE136961, GSE140901, GSE165252, GSE165278, GSE176307, GSE183924, GSE78220, GSE91061, LIU2019, MARIATHASAN2018, and VANALLEN2015. For PFS, these data originated from the following: GIDE2019, GSE121810, GSE136961, GSE140901, GSE165252, GSE176307, GSE183924, GSE93157, LIU2019, and VANALLEN2015. Here, 100% coverage of the above TAM signature was prioritized over accommodation of all patients from within these cohorts, thereby resulting in the analyses of 129 patients for PFS and 152 patients for OS. This is because not all cohorts captured all the genes relevant for our signature due to differences in profiling and processing methods across the studies. Final analyses entailed creation of Kaplan-Meier curves, at autoselect best cutoff (13,505.31 gene expression value, within the range of 3406 to 42,051 for OS, and 12,834.6 gene expression value, within the range of 3406 to 29,188 for PFS) with univariate Cox regression and log-rank *P* value analyses.

Flow cytometry analysis via Pytometry

Our existing FACS data was reanalyzed through Pytometry 0.1.3. Values were arcsinh transformed and gated in accordance with our analysis via FlowJo (see the Supplementary Materials for gating strategies) to select subtypes. The principal components analysis space was built with five components, while the number of closest neighbors was defined as 15. Neighbor calculation and Leiden clustering (Leidenalg 0.9.1) was performed with ScanPy 1.9.3 and projected as Uniform Manifold Approximation and Projection (UMAP) with Umap-learn 0.5.3. Kernel Density Estimate (KDE) plots were generated using Seaborn 0.12.2 and Matplotlib 3.7.1.

Correlation analysis

Single-cell transcriptomic profiles of 2,489,382 MΦs were integrated and annotated from 1679 scRNA-seq studies of human origin (pan-disease or pan-tissue) and analyzed using the Talk2Data Database v.4.0. Talk2Data's coexpression function was used to calculate a dotplot (scale mode: relative) of the top most correlated (Jaccard's index) genes among *HAVCR2*, *VSIR*, *SPP1*, *MRC1*, *ARG1*, *CD163*, *CSF1R*, *TREM2*, *TEK*, *IL10*, *TIMP1*, *PDGFB*, *TGIF1*, *ITGAX*, *IRF3*, *STAT1*, *IL1B*, *FOLR2*, *LYVE1*, *TNF*, *CCL2*, *MMP2*, *MMP9*, *IL6*, *CXCL10*, and *CR1* in 2,489,382 cells in MΦs. The Jaccard's index between two genes g1 and g2 is calculated as follows: Jaccard's index (g1, g2) = (number of cells that express both g1 and g2) / (number of cells that express at least one of the two genes).

Statistical analysis

The statistical details of all the analyses are reported in the figure legends, figures, and/or Materials and Methods, including statistical analysis performed, statistical significance thresholds/values, and, in most cases, the counts/number of data points. All statistical analyses were performed using GraphPad Prism software. Statistical significance was calculated by two-tailed unpaired Mann-Whitney test on two experimental conditions and Kruskal-Wallis test with multiple comparisons correction for false discovery rate (FDR) with two-stage step-up method of Benjamini, Krieger, and Yekutieli when more than two experimental groups were compared. Multiple comparison was always done to PBS/UT or to the indicated controls in the graphs. Gene signatures were estimated by considering the average expression of all the genes within that signature, unless otherwise mentioned. Details about used software for analysis can be found in the Supplementary Materials.

Study approval

Mouse experiments were approved by the animal ethics committee at KU Leuven (projects P114/2019 and p195/2020) following the European directive 2010/63/EU as amended by the Regulation (European Union) 2019/1010 and the Flemish government decree of 17 February 2017.

Supplementary Materials

This PDF file includes:

Figs. S1 to S14
Tables S1 and S2
Gating strategies
Western blots

REFERENCES AND NOTES

1. S. C. Wei, C. R. Duffy, J. P. Allison, Fundamental mechanisms of immune checkpoint blockade therapy. *Cancer Discov.* **8**, 1069–1086 (2018).
2. P. Sharma, J. P. Allison, Dissecting the mechanisms of immune checkpoint therapy. *Nat. Rev. Immunol.* **20**, 75–76 (2020).
3. A. J. Schoenfeld, M. D. Hellmann, Acquired resistance to immune checkpoint inhibitors. *Cancer Cell* **37**, 443–455 (2020).
4. P. Sharma, S. Hu-Lieskovan, J. A. Wargo, A. Ribas, Primary, adaptive, and acquired resistance to cancer immunotherapy. *Cell* **168**, 707–723 (2017).
5. T. R. Medler, T. C. Blair, M. R. Crittenden, M. J. Gough, Defining immunogenic and radioimmunogenic tumors. *Front. Oncol.* **11**, 667075 (2021).
6. P. Sharma, B. A. Siddiqui, S. Anandhan, S. S. Yadav, S. K. Subudhi, J. Gao, S. Goswami, J. P. Allison, The next decade of immune checkpoint therapy. *Cancer Discov.* **11**, 838–857 (2021).
7. J. Niu, C. Maurice-Dror, D. H. Lee, D. W. Kim, A. Nagrial, M. Voskoboynik, H. C. Chung, K. Mileham, U. Vaishampayan, D. Rasco, T. Golan, T. M. Bauer, A. Jimeno, V. Chung, E. Chartash, M. Lala, Q. Chen, J. A. Healy, M. J. Ahn, First-in-human phase 1 study of the anti-TIGIT antibody vibostolimab as monotherapy or with pembrolizumab for advanced solid tumors, including non-small-cell lung cancer☆. *Ann. Oncol.* **33**, 169–180 (2022).
8. D. H. Lee, Update of early phase clinical trials in cancer immunotherapy. *BMB Rep.* **54**, 70–88 (2021).
9. G. Curigliano, H. Gelderblom, N. Mach, T. Doi, D. Tai, P. M. Forde, J. Sarantopoulos, P. L. Bedard, C.-C. Lin, F. S. Hodi, S. Wilgenhof, A. Santoro, C. A. Sabatos-Peyton, T. A. Longmire, A. Xyrafas, H. Sun, S. Gutzwiller, L. Manenti, A. Naing, Phase I/Ib clinical trial of sabatolimab, an anti-TIM-3 antibody, alone and in combination with spartalizumab, an anti-PD-1 antibody, in advanced solid tumors. *Clin. Cancer Res.* **27**, 3620–3629 (2021).
10. C. Gomez-Roca, S. Champiat, P. Cassier, D. Jegou, M. Primard, A. Pétain, G. Gueguen-Dorbes, C. Fabre, I. Melero, A. Marabelle, Abstract CT181: First-in-human phase I of anti-VISTA monoclonal antibody W0180 with and without anti-PD-1 pembrolizumab in patients with locally advanced or metastatic solid tumors. *Cancer Res.* **84**, CT181 (2024).
11. M. Chalabi, L. F. Fanchi, K. K. Dijkstra, J. G. Van den Berg, A. G. Aalbers, K. Sikorska, M. Lopez-Yurda, C. Grootscholten, G. L. Beets, P. Snaebjornsson, M. Maas, M. Mertz, V. Veninga, G. Bounova, A. Broeks, R. G. Beets-Tan, T. R. de Wijkerslooth, A. U. van Lent, H. A. Marsman, E. Nuijten, N. F. Kok, M. Kuiper, W. H. Verbeek, M. Kok, M. E. Van Leerdam, T. N. Schumacher, E. E. Voest, J. B. Haanen, Neoadjuvant immunotherapy leads to pathological responses in MMR-proficient and MMR-deficient early-stage colon cancers. *Nat. Med.* **26**, 566–576 (2020).
12. R. S. Laureano, I. Vanmeerbeek, J. Sprooten, J. Govaerts, S. Naulaerts, A. D. Garg, The cell stress and immunity cycle in cancer: Toward next generation of cancer immunotherapy. *Immunol. Rev.* **321**, 71–93 (2024).
13. K. Nakamura, M. J. Smyth, Myeloid immunosuppression and immune checkpoints in the tumor microenvironment. *Cell. Mol. Immunol.* **17**, 1–12 (2020).
14. S.-Y. Park, I.-S. Kim, Harnessing immune checkpoints in myeloid lineage cells for cancer immunotherapy. *Cancer Lett.* **452**, 51–58 (2019).
15. S. R. Gordon, R. L. Maute, B. W. Dulken, G. Hutter, B. M. George, M. N. McCracken, R. Gupta, J. M. Tsai, R. Sinha, D. Corey, A. M. Ring, A. J. Connolly, I. L. Weissman, PD-1 expression by tumour-associated macrophages inhibits phagocytosis and tumour immunity. *Nature* **545**, 495–499 (2017).
16. A. Mantovani, P. Allavena, F. Marchesi, C. Garlanda, Macrophages as tools and targets in cancer therapy. *Nat. Rev. Drug Discov.* **21**, 799–820 (2022).
17. E. Schaafsma, W. Croteau, M. ElTanbouly, E. C. Nowak, N. C. Smits, J. Deng, A. Sarde, C. A. Webber, D. Rabadi, C. Cheng, R. Noelle, J. L. Lines, VISTA targeting of T-cell quiescence and myeloid suppression overcomes adaptive resistance. *Cancer Immunol. Res.* **11**, 38–55 (2023).
18. Á. de Mingo Pulido, K. Hänggi, D. P. Celias, A. Gardner, J. Li, B. Batista-Bittencourt, E. Mohamed, J. Trillo-Tinoco, O. Osunmakinde, R. Peña, A. Onimus, T. Kaisho, J. Kaufmann, K. McEachern, H. Soliman, V. C. Luca, P. C. Rodriguez, X. Yu, B. Ruffell, The inhibitory receptor TIM-3 limits activation of the cGAS-STING pathway in intra-tumoral dendritic cells by suppressing extracellular DNA uptake. *Immunity* **54**, 1154–1167.e7 (2021).
19. A. Gardner, Á. de Mingo Pulido, K. Hänggi, S. Bazargan, A. Onimus, A. Kasprzak, J. R. Conejo-Garcia, K. A. Rejniak, B. Ruffell, TIM-3 blockade enhances IL-12-dependent antitumor immunity by promoting CD8$^+$ T cell and XCR1$^+$ dendritic cell spatial co-localization. *J. Immunother. Cancer* **10**, e003571 (2022).
20. S. Naulaerts, A. Datsi, D. M. Borras, A. Antoranz Martinez, J. Messiaen, I. Vanmeerbeek, J. Sprooten, R. S. Laureano, J. Govaerts, D. Panovska, M. Derweduwe, M. C. Sabel, M. Rapp, W. Ni, S. Mackay, Y. Van Herck, L. Gelens, T. Venken, S. More, O. Bechter, G. Bergers, A. Liston, S. De Vleeschouwer, B. J. Van Den Eynde, D. Lambrechts, M. Verfaillie, F. Bosisio, S. Tejpar, J. Borst, R. V. Sorg, F. De Smet, A. D. Garg, Multiomics and spatial mapping characterizes human CD8$^+$ T cell states in cancer. *Sci. Transl. Med.* **15**, eadd1016 (2023).
21. J. Sprooten, A. Vankerckhoven, I. Vanmeerbeek, D. M. Borras, Y. Berckmans, R. Wouters, R. S. Laureano, T. Baert, L. Boon, C. Landolfo, A. C. Testa, D. Fischerova, C. Van Holsbeke, T. Bourne, V. Chiappa, W. Froyman, D. Schols, P. Agostinis, D. Timmerman, S. Tejpar, I. Vergote, A. Coosemans, A. D. Garg, Peripherally-driven myeloid NFkB and IFN/ISG responses predict malignancy risk, survival, and immunotherapy regime in ovarian cancer. *J. Immunother. Cancer* **9**, e003609 (2021).
22. D. M. Borràs, S. Verbandt, M. Ausserhofer, G. Sturm, J. Lim, G. A. Verge, I. Vanmeerbeek, R. S. Laureano, J. Govaerts, J. Sprooten, Y. Hong, R. Wall, G. De Hertogh, X. Sagaert, G. Bislenghi, A. D'Hoore, A. Wolthuis, F. Finotello, W.-Y. Park, S. Naulaerts, S. Tejpar, A. D. Garg, Single cell dynamics of tumor specificity vs bystander activity in CD8$^+$ T cells define the diverse immune landscapes in colorectal cancer. *Cell Discov.* **9**, 114 (2023).
23. A. Chow, K. Perica, C. A. Klebanoff, J. D. Wolchok, Clinical implications of T cell exhaustion for cancer immunotherapy. *Nat. Rev. Clin. Oncol.* **19**, 775–790 (2022).
24. M. Sade-Feldman, K. Yizhak, S. L. Bjorgaard, J. P. Ray, C. G. de Boer, R. W. Jenkins, D. J. Lieb, J. H. Chen, D. T. Frederick, M. Barzily-Rokni, S. S. Freeman, A. Reuben, P. J. Hoover, A.-C. Villani, E. Ivanova, A. Portell, P. H. Lizotte, A. R. Aref, J.-P. Eliane, M. R. Hammond, H. Vitzthum, S. M. Blackmon, B. Li, V. Gopalakrishnan, S. M. Reddy, Z. A. Cooper, C. P. Paweletz, D. A. Barbie, A. Stemmer-Rachamimov, K. T. Flaherty, J. A. Wargo, G. M. Boland, R. J. Sullivan, G. Getz, N. Hacohen, Defining T cell states associated with response to checkpoint immunotherapy in melanoma. *Cell* **175**, 998–1013.e20 (2018).
25. T. D. Wu, S. Madireddi, P. E. de Almeida, R. Banchereau, Y.-J. J. Chen, A. S. Chitre, E. Y. Chiang, H. Iftikhar, W. E. O'Gorman, A. Au-Yeung, C. Takahashi, L. D. Goldstein, C. Poon, S. Keerthivasan, D. E. de Almeida Nagata, X. Du, H.-M. Lee, K. L. Banta, S. Mariathasan, M. Das Thakur, M. A. Huseni, M. Ballinger, I. Estay, P. Caplazi, Z. Modrusan, L. Delamarre, I. Mellman, R. Bourgon, J. L. Grogan, Peripheral T cell expansion predicts tumour infiltration and clinical response. *Nature* **579**, 274–278 (2020).
26. K. Mulder, A. A. Patel, W. T. Kong, C. Piot, E. Halitzki, G. Dunsmore, S. Khalilnezhad, S. E. Irac, A. Dubuisson, M. Chevrier, X. M. Zhang, J. K. C. Tam, T. K. H. Lim, R. M. M. Wong, R. Pai, A. I. S. Khalil, P. K. H. Chow, S. Z. Wu, G. Al-Eryani, D. Roden, A. Swarbrick, J. K. Y. Chan, S. Albani, L. Derosa, L. Zitvogel, A. Sharma, J. Chen, A. Silvin, A. Bertoletti, C. Blériot, C.-A. Dutertre, F. Ginhoux, Cross-tissue single-cell landscape of human monocytes and macrophages in health and disease. *Immunity* **54**, 1883–1900.e5 (2021).
27. H.-O. Lee, Y. Hong, H. E. Etlioglu, Y. B. Cho, V. Pomella, B. Van den Bosch, J. Vanhecke, S. Verbandt, H. Hong, J.-W. Min, N. Kim, H. H. Eum, J. Qian, B. Boeckx, D. Lambrechts, P. Tsantoulis, G. De Hertogh, W. Chung, T. Lee, M. An, H.-T. Shin, J.-G. Joung, M.-H. Jung, G. Ko, P. Wirapati, S. H. Kim, H. C. Kim, S. H. Yun, I. B. H. Tan, B. Ranjan, W. Y. Lee, T.-Y. Kim, J. K. Choi, Y.-J. Kim, S. Prabhakar, S. Tejpar, W.-Y. Park, Lineage-dependent gene expression programs influence the immune landscape of colorectal cancer. *Nat. Genet.* **52**, 594–603 (2020).
28. S. Wang, R. Song, Z. Wang, Z. Jing, S. Wang, J. Ma, S100A8/A9 in inflammation. *Front. Immunol.* **9**, 1298 (2018).
29. T. Lawrence, G. Natoli, Transcriptional regulation of macrophage polarization: Enabling diversity with identity. *Nat. Rev. Immunol.* **11**, 750–761 (2011).
30. P. J. Murray, T. A. Wynn, Protective and pathogenic functions of macrophage subsets. *Nat. Rev. Immunol.* **11**, 723–737 (2011).
31. A. Ghate, S. Sharma, P. Agrawal, A. Sahu, Differential expression of complement receptors CR1/2 and CR4 by murine M1 and M2 macrophages. *Mol. Immunol.* **137**, 75–83 (2021).
32. G. Chinetti-Gbaguidi, S. Colin, B. Staels, Macrophage subsets in atherosclerosis. *Nat. Rev. Cardiol.* **12**, 10–17 (2015).
33. P. Rodríguez-Morales, R. A. Franklin, Macrophage phenotypes and functions: Resolving inflammation and restoring homeostasis. *Trends Immunol.* **44**, 986–998 (2023).
34. I. Nasir, C. McGuinness, A. R. Poh, M. Ernst, P. K. Darcy, K. L. Britt, Tumor macrophage functional heterogeneity can inform the development of novel cancer therapies. *Trends Immunol.* **44**, 971–985 (2023).
35. T. Le, T. Phan, M. Pham, D. Tran, L. Lam, T. Nguyen, T. Truong, H. Vuong, T. Luu, N. Phung, T. Nguyen, O. Pham, A. Nguyen, H. Nguyen, H. Tran, L. Tran, H. A. Nguyen, T. Tran, N. Nguyen, N. Tran, C. Boysen, U. Nguyen, V. Pham, K. Theodore, N. Pham, T. Gill, S. Pham, BBrowser: Making single-cell data easily accessible. bioRxiv 2020.12.11.414136 [Preprint] (2020). https://doi.org/10.1101/2020.12.11.414136.
36. C. Salvagno, M. Ciampricotti, S. Tuit, C.-S. Hau, A. van Weverwijk, S. B. Coffelt, K. Kersten, K. Vrijland, K. Kos, T. Ulas, J.-Y. Song, C.-H. Ooi, D. Rüttinger, P. A. Cassier, J. Jonkers, J. L. Schultze, C. H. Ries, K. E. de Visser, Therapeutic targeting of macrophages enhances chemotherapy efficacy by unleashing type I interferon response. *Nat. Cell Biol.* **21**, 511–521 (2019).
37. S. I. S. Mosely, J. E. Prime, R. C. A. Sainson, J.-O. Koopmann, D. Y. Q. Wang, D. M. Greenawalt, M. J. Ahdesmaki, R. Leyland, S. Mullins, L. Pacelli, D. Marcus, J. Anderton, A. Watkins, J. Coates Ulrichsen, P. Brohawn, B. W. Higgs, M. McCourt, H. Jones, J. A. Harper, M. Morrow, V. Valge-Archer, R. Stewart, S. J. Dovedi, R. W. Wilkinson, Rational selection of syngeneic preclinical tumor models for immunotherapeutic drug discovery. *Cancer Immunol. Res.* **5**, 29–41 (2017).
38. A. Murgaski, M. Kiss, H. Van Damme, D. Kancheva, I. Vanmeerbeek, J. Keirsse, E. Hadadi, J. Brughmans, S. M. Arnouk, A. E. I. Hamouda, A. Debraekeleer, V. Bosteels, Y. Elkrim,

L. Boon, S. Hoves, N. Vandamme, S. Deschoemaeker, S. Janssens, A. D. Garg, G. Vande Velde, M. Schmittnaegel, C. H. Ries, D. Laoui, Efficacy of CD40 agonists is mediated by distinct cDC subsets and subverted by suppressive macrophages. *Cancer Res.* **82**, 3785–3801 (2022).

39. M. Feng, W. Jiang, B. Y. S. Kim, C. C. Zhang, Y.-X. Fu, I. L. Weissman, Phagocytosis checkpoints as new targets for cancer immunotherapy. *Nat. Rev. Cancer* **19**, 568–586 (2019).
40. G. Kroemer, C. Galassi, L. Zitvogel, L. Galluzzi, Immunogenic cell stress and death. *Nat. Immunol.* **23**, 487–500 (2022).
41. A. D. Garg, E. Romano, N. Rufo, P. Agostinis, Immunogenic versus tolerogenic phagocytosis during anticancer therapy: Mechanisms and clinical translation. *Cell Death Differ.* **23**, 938–951 (2016).
42. I. Vanmeerbeek, J. Sprooten, D. De Ruysscher, S. Tejpar, P. Vandenberghe, J. Fucikova, R. Spisek, L. Zitvogel, G. Kroemer, L. Galluzzi, A. D. Garg, Trial watch: Chemotherapy-induced immunogenic cell death in immuno-oncology. *Oncoimmunology* **9**, 1703449 (2020).
43. A. D. Garg, L. Vandenberk, S. Fang, T. Fasche, S. Van Eygen, J. Maes, M. Van Woensel, C. Koks, N. Vanthillo, N. Graf, P. de Witte, S. Van Gool, P. Salven, P. Agostinis, Pathogen response-like recruitment and activation of neutrophils by sterile immunogenic dying cells drives neutrophil-mediated residual cell killing. *Cell Death Differ.* **24**, 832–843 (2017).
44. L. Galluzzi, I. Vitale, S. Warren, S. Adjemian, P. Agostinis, A. B. Martinez, T. A. Chan, G. Coukos, S. Demaria, E. Deutsch, D. Draganov, R. L. Edelson, S. C. Formenti, J. Fucikova, L. Gabriele, U. S. Gaipl, S. R. Gameiro, A. D. Garg, E. Golden, J. Han, K. J. Harrington, A. Hemminki, J. W. Hodge, D. M. S. Hossain, T. Illidge, M. Karin, H. L. Kaufman, O. Kepp, G. Kroemer, J. J. Lasarte, S. Loi, M. T. Lotze, G. Manic, T. Merghoub, A. A. Melcher, K. L. Mossman, F. Prosper, Ø. Rekdal, M. Rescigno, C. Riganti, A. Sistigu, M. J. Smyth, R. Spisek, J. Stagg, B. E. Strauss, D. Tang, K. Tatsuno, S. W. van Gool, P. Vandenabeele, T. Yamazaki, D. Zamarin, L. Zitvogel, A. Cesano, F. M. Marincola, Consensus guidelines for the definition, detection and interpretation of immunogenic cell death. *J. Immunother. Cancer* **8**, e000337 (2020).
45. T. Nguyen, J. Du, Y. C. Li, A protocol for macrophage depletion and reconstitution in a mouse model of sepsis. *STAR Protoc.* **2**, 101004 (2021).
46. S. Chen, A. F. U. H. Saeed, Q. Liu, Q. Jiang, H. Xu, G. G. Xiao, L. Rao, Y. Duo, Macrophages in immunoregulation and therapeutics. *Signal Transduct. Target. Ther.* **8**, 207 (2023).
47. T. Yang, B. W. Poovaiah, Hydrogen peroxide homeostasis: Activation of plant catalase by calcium/calmodulin. *Proc. Natl. Acad. Sci. U.S.A.* **99**, 4097–4102 (2002).
48. K. Kashfi, J. Kannikal, N. Nath, Macrophage reprogramming and cancer therapeutics: Role of iNOS-derived NO. *Cells* **10**, 3194 (2021).
49. N. Anand, K. H. Peh, J. M. Kolesar, Macrophage repolarization as a therapeutic strategy for osteosarcoma. *Int. J. Mol. Sci.* **24**, 2858 (2023).
50. J. Sprooten, I. Vanmeerbeek, A. Datsi, J. Govaerts, S. Naulaerts, R. S. Laureano, D. M. Borràs, A. Calvet, V. Malviya, M. Kuballa, J. Felsberg, M. C. Sabel, M. Rapp, C. Knobbe-Thomsen, P. Liu, L. Zhao, O. Kepp, L. Boon, S. Tejpar, J. Borst, G. Kroemer, S. Schlenner, S. De Vleeschouwer, R. V. Sorg, A. D. Garg, Lymph node and tumor-associated PD-L1$^+$ macrophages antagonize dendritic cell vaccines by suppressing CD8$^+$ T cells. *Cell Rep. Med.* **5**, 101377 (2024).
51. R. L. Gieseck, M. S. Wilson, T. A. Wynn, Type 2 immunity in tissue repair and fibrosis. *Nat. Rev. Immunol.* **18**, 62–76 (2018).
52. M. Łuksza, N. Riaz, V. Makarov, V. P. Balachandran, M. D. Hellmann, A. Solovyov, N. A. Rizvi, T. Merghoub, A. J. Levine, T. A. Chan, J. D. Wolchok, B. D. Greenbaum, A neoantigen fitness model predicts tumour response to checkpoint blockade immunotherapy. *Nature* **551**, 517–520 (2017).
53. A. Sistigu, T. Yamazaki, E. Vacchelli, K. Chaba, D. P. Enot, J. Adam, I. Vitale, A. Goubar, E. E. Baracco, C. Remédios, L. Fend, D. Hannani, L. Aymeric, Y. Ma, M. Niso-Santano, O. Kepp, J. L. Schultze, T. Tüting, F. Belardelli, L. Bracci, V. La Sorsa, G. Ziccheddu, P. Sestili, F. Urbani, M. Delorenzi, M. Lacroix-Triki, V. Quidville, R. Conforti, J.-P. Spano, L. Pusztai, V. Poirier-Colame, S. Delaloge, F. Penault-Llorca, S. Ladoire, L. Arnould, J. Cyrta, M.-C. Dessoliers, A. Eggermont, M. E. Bianchi, M. Pittet, C. Engblom, C. Pfirschke, X. Préville, G. Uzè, R. D. Schreiber, M. T. Chow, M. J. Smyth, E. Proietti, F. André, G. Kroemer, L. Zitvogel, Cancer cell-autonomous contribution of type I interferon signaling to the efficacy of chemotherapy. *Nat. Med.* **20**, 1301–1309 (2014).
54. N. Acharya, C. Sabatos-Peyton, A. C. Anderson, Tim-3 finds its place in the cancer immunotherapy landscape. *J. Immunother. Cancer* **8**, e000911 (2020).
55. L. Yuan, J. Tatineni, K. M. Mahoney, G. J. Freeman, VISTA: A mediator of quiescence and a promising target in cancer immunotherapy. *Trends Immunol.* **42**, 209–227 (2021).
56. K. W. Yoon, S. Byun, E. Kwon, S.-Y. Hwang, K. Chu, M. Hiraki, S.-H. Jo, A. Weins, S. Hakroush, A. Cebulla, D. B. Sykes, A. Greka, P. Mundel, D. E. Fisher, A. Mandinova, S. W. Lee, Control of signaling-mediated clearance of apoptotic cells by the tumor suppressor p53. *Science* **349**, 1261669 (2015).
57. K. Meeth, J. X. Wang, G. Micevic, W. Damsky, M. W. Bosenberg, The YUMM lines: A series of congenic mouse melanoma cell lines with defined genetic alterations. *Pigment Cell Melanoma Res.* **29**, 590–597 (2016).
58. J. Wang, C. J. Perry, K. Meeth, D. Thakral, W. Damsky, G. Micevic, S. Kaech, K. Blenman, M. Bosenberg, UV-induced somatic mutations elicit a functional T cell response in the YUMMER1.7 mouse melanoma model. *Pigment Cell Melanoma Res.* **30**, 428–435 (2017).
59. M. Rumpret, J. Drylewicz, L. J. E. Ackermans, J. A. M. Borghans, R. Medzhitov, L. Meyaard, Functional categories of immune inhibitory receptors. *Nat. Rev. Immunol.* **20**, 771–780 (2020).
60. S. Goswami, S. Anandhan, D. Raychaudhuri, P. Sharma, Myeloid cell-targeted therapies for solid tumours. *Nat. Rev. Immunol.* **23**, 106–120 (2023).
61. S. Kalaora, A. Nagler, J. A. Wargo, Y. Samuels, Mechanisms of immune activation and regulation: Lessons from melanoma. *Nat. Rev. Cancer* **22**, 195–207 (2022).
62. Á. de Mingo Pulido, A. Gardner, S. Hiebler, H. Soliman, H. S. Rugo, M. F. Krummel, L. M. Coussens, B. Ruffell, TIM-3 regulates CD103$^+$ dendritic cell function and response to chemotherapy in breast cancer. *Cancer Cell* **33**, 60–74.e6 (2018).
63. H. Li, Y. Xiao, Q. Li, J. Yao, X. Yuan, Y. Zhang, X. Yin, Y. Saito, H. Fan, P. Li, W.-L. Kuo, A. Halpin, D. L. Gibbons, H. Yagita, Z. Zhao, D. Pang, G. Ren, C. Yee, J. J. Lee, D. Yu, The allergy mediator histamine confers resistance to immunotherapy in cancer patients via activation of the macrophage histamine receptor H1. *Cancer Cell* **40**, 36–52.e9 (2022).
64. W. Celus, A. I. Oliveira, S. Rivis, H. H. Van Acker, E. Landeloos, J. Serneels, S. T. Cafarello, Y. Van Herck, R. Mastrantonio, A. Köhler, A. D. Garg, V. Flamand, L. Tamagnone, J.-C. Marine, M. Di Matteo, B. M. Costa, O. Bechter, M. Mazzone, Plexin-A4 mediates cytotoxic T-cell trafficking and exclusion in cancer. *Cancer Immunol. Res.* **10**, 126–141 (2022).
65. N. E. Sanjana, O. Shalem, F. Zhang, Improved vectors and genome-wide libraries for CRISPR screening. *Nat. Methods* **11**, 783–784 (2014).
66. J. Shang, G. Ye, K. Shi, Y. Wan, C. Luo, H. Aihara, Q. Geng, A. Auerbach, F. Li, Structural basis of receptor recognition by SARS-CoV-2. *Nature* **581**, 221–224 (2020).
67. R. Edgar, M. Domrachev, A. E. Lash, Gene Expression Omnibus: NCBI gene expression and hybridization array data repository. *Nucleic Acids Res.* **30**, 207–210 (2002).
68. B. S. Carvalho, R. A. Irizarry, A framework for oligonucleotide microarray preprocessing. *Bioinformatics* **26**, 2363–2367 (2010).
69. "R: The R project for statistical computing", [Accessed 30 May 2024]; www.r-project.org/.
70. M. E. Ritchie, B. Phipson, D. Wu, Y. Hu, C. W. Law, W. Shi, G. K. Smyth, limma powers differential expression analyses for RNA-sequencing and microarray studies. *Nucleic Acids Res.* **43**, e47 (2015).
71. J. Vivian, A. A. Rao, F. A. Nothaft, C. Ketchum, J. Armstrong, A. Novak, J. Pfeil, J. Narkizian, A. D. Deran, A. Musselman-Brown, H. Schmidt, P. Amstutz, B. Craft, M. Goldman, K. Rosenbloom, M. Cline, B. O'Connor, M. Hanna, C. Birger, W. J. Kent, D. A. Patterson, A. D. Joseph, J. Zhu, S. Zaranek, G. Getz, D. Haussler, B. Paten, Toil enables reproducible, open source, big biomedical data analyses. *Nat. Biotechnol.* **35**, 314–316 (2017).
72. M. J. Goldman, B. Craft, M. Hastie, K. Repečka, F. McDade, A. Kamath, A. Banerjee, Y. Luo, D. Rogers, A. N. Brooks, J. Zhu, D. Haussler, Visualizing and interpreting cancer genomics data via the Xena platform. *Nat. Biotechnol.* **38**, 675–678 (2020).
73. V. Thorsson, D. L. Gibbs, S. D. Brown, D. Wolf, D. S. Bortone, T.-H. O. Yang, E. Porta-Pardo, G. F. Gao, C. L. Plaisier, J. A. Eddy, E. Ziv, A. C. Culhane, E. O. Paull, I. K. A. Sivakumar, A. J. Gentles, R. Malhotra, F. Farshidfar, A. Colaprico, J. S. Parker, L. E. Mose, N. S. Vo, J. Liu, Y. Liu, J. Rader, V. Dhankani, S. M. Reynolds, R. Bowlby, A. Califano, A. D. Cherniack, D. Anastassiou, D. Bedognetti, Y. Mokrab, A. M. Newman, A. Rao, K. Chen, A. Krasnitz, H. Hu, T. M. Malta, H. Noushmehr, C. S. Pedamallu, S. Bullman, A. I. Ojesina, A. Lamb, W. Zhou, H. Shen, T. K. Choueiri, J. N. Weinstein, J. Guinney, J. Saltz, R. A. Holt, C. S. Rabkin, Cancer Genome Atlas Research Network, A. J. Lazar, J. S. Serody, E. G. Demicco, M. L. Disis, B. G. Vincent, I. Shmulevich, The immune landscape of cancer. *Immunity* **48**, 812–830.e14 (2018).
74. T. Li, J. Fu, Z. Zeng, D. Cohen, J. Li, Q. Chen, B. Li, X. S. Liu, TIMER2.0 for analysis of tumor-infiltrating immune cells. *Nucleic Acids Res.* **48**, W509–W514 (2020).
75. F. Finotello, C. Mayer, C. Plattner, G. Laschober, D. Rieder, H. Hackl, A. Krogsdam, Z. Loncova, W. Posch, D. Wilflingseder, S. Sopper, M. Ijsselsteijn, T. P. Brouwer, D. Johnson, Y. Xu, Y. Wang, M. E. Sanders, M. V. Estrada, P. Ericsson-Gonzalez, P. Charoentong, J. Balko, N. F. C. C. de Miranda, Z. Trajanoski, Molecular and pharmacological modulators of the tumor immune contexture revealed by deconvolution of RNA-seq data. *Genome Med.* **11**, 34 (2019).
76. "SciPy - Citing SciPy", [Accessed 30 May 2024]; https://scipy.org/citing-scipy/.
77. J. D. Hunter, Matplotlib: A 2D graphics environment. *Comput. Sci. Eng.* **9**, 90–95 (2007).
78. "Citing lifelines—Lifelines 0.27.4 documentation," August 2019; https://lifelines.readthedocs.io/en/stable/Citing%20lifelines.html.
79. A. Lánczky, B. Győrffy, Web-based survival analysis tool tailored for medical research (KMplot): Development and implementation. *J. Med. Internet Res.* **23**, e27633 (2021).
80. S. A. Kovács, B. Győrffy, Transcriptomic datasets of cancer patients treated with immune-checkpoint inhibitors: A systematic review. *J. Transl. Med.* **20**, 249 (2022).

Acknowledgments: We are thankful to R. Vandenbroucke (VIB-UGent) for providing us with the *Ifnar1*$^{-/-}$ C57BL/6 mice. We acknowledge P. Agostinis, G. Bultynck, and P. Vangheluwe (KU Leuven, Belgium) for supporting our research by sharing laboratory space and/or cell culture facilities. We would like to thank K. Minner for essential technical support and the KU Leuven

FACS CORE for assistance in flow cytometry and especially V. Dermesrobian and B. Moraschi for the excellent assistance with sorting cells. **Funding:** This study is supported by Research Foundation Flanders (FWO) (Fundamental Research grant G0B4620N to A.D.G. and Excellence of Science/EOS grant 30837538 for "DECODE" consortium to A.D.G.), KU Leuven (C1 grant C14/19/098, C3 grants C3/21/037 and C3/23/067, and POR award funds POR/16/040 to A.D.G.), Kom op Tegen Kanker (KOTK/2018/11509/1 and KOTK/2019/11955/1 to A.D.G.), and VLIR-UOS (iBOF grant iBOF/21/048 for "MIMICRY" consortium to A.D.G. and S.T.). I.V. and R.S.L. are supported by FWO-SB PhD Fellowship (1S06821N and 1S44123N). J.S. is funded by Kom op tegen Kanker (Stand up to Cancer), the Flemish cancer society through the Emmanuel van der Schueren (EvDS) PhD fellowship (project ID: 12699), and KU Leuven's Postdoctoral Mandate (PDM) fellowship (PDMT2/23/071). S.N. is funded by Stichting tegen Kanker Postdoctoral fellowship (2023-046). **Author contributions:** Conceptualization: S.T., R.S.L., I.V., and A.D.G. Methodology: L.B., S.M.S., M.J., R.T., S.T., J.S., M.M., S.Z., J.G., S.P., S.T.C., I.V., and A.D.G. Data curation: M.J., M.M., S.N., I.V., and A.D.G. Validation: S.M.S., M.J., J.S., M.M., J.G., S.T.C., I.V., and A.D.G. Investigation: M.J., R.T., M.P., J.S., J.V., S.Z., J.G., S.P., S.T.C., I.V., and A.D.G. Formal analysis: S.T., S.N., I.V., and A.D.G. Resources: L.B., S.M.S., M.J., S.T., M.M., J.G., S.T.C., I.V., and A.D.G. Software: S.N. and I.V. Visualization: M.J., J.S., M.M., R.S.L., J.G., I.V., and A.D.G. Writing (original draft): S.T., R.S.L., I.V., and A.D.G. Writing (reviewing and editing): L.B., S.M.S., J.S., M.M., S.N., R.S.L., J.G., I.V., and A.D.G. Project administration: M.M., I.V., and A.D.G. Supervision: I.V., S.T., D.D., and A.D.G. Funding acquisition: I.V. and A.D.G. **Competing interests:** A.D.G. received consulting/advisory/lecture honoraria from Boehringer Ingelheim (Germany), Miltenyi Biotec (Germany), Novigenix (Switzerland), Sotio (Czech Republic), and IsoPlexis (USA). A.D.G. and I.V. are inventors on a patent application relating to this research, filed in the name of Katholieke Universiteit Leuven, which is pending at the time of submission of this manuscript. All other authors declare that they have no competing interests. **Data and materials availability:** All data needed to evaluate the conclusions in the paper are present in the paper and/or the Supplementary Materials.

Submitted 9 November 2023
Accepted 14 June 2024
Published 19 July 2024
10.1126/sciadv.adm8660